The Relationship between Equatorial Mixed Rossby–Gravity and Eastward Inertio-Gravity Waves. Part I

GEORGE N. KILADIS

Physical Sciences Division, NOAA/Earth System Research Laboratory, Boulder, Colorado

JULIANA DIAS AND MARIA GEHNE

CIRES, University of Colorado Boulder, and NOAA/Earth System Research Laboratory, Boulder, Colorado

(Manuscript received 7 August 2015, in final form 28 December 2015)

ABSTRACT

The relationship between $n = 0$ mixed Rossby–gravity waves (MRGs) and eastward inertio-gravity waves (EIGs) from Matsuno's shallow-water theory on an equatorial beta plane is studied using statistics of satellite brightness temperature T_b and dynamical fields from ERA-Interim data. Unlike other observed convectively coupled equatorial waves, which have spectral signals well separated into eastward and westward modes, there is a continuum of MRG–EIG power standing above the background that peaks near wavenumber 0. This continuum is also present in the signals of dry stratospheric MRGs. While hundreds of papers have been written on MRGs, very little work on EIGs has appeared in the literature to date. The authors attribute this to the fact that EIG circulations are much weaker than those of MRGs for a given amount of divergence, making them more difficult to observe even though they strongly modulate convection.

Empirical orthogonal function (EOF) and cross-spectral analysis of 2–6-day-filtered T_b isolate zonally standing modes of synoptic-scale convection originally identified by Wallace in 1971. These display antisymmetric T_b signals about the equator that propagate poleward with a period of around 4 days, along with westward-propagating MRG-like circulations that move through the T_b patterns. Further analysis here and in Part II shows that these signatures are not artifacts of the EOF approach but result from a mixture of MRG or EIG modes occurring either in isolation or at the same time.

1. Introduction

Mixed Rossby–gravity waves (MRGs) were the first equatorially trapped waves predicted by theory (Rattray 1965; Rosenthal 1965; Blandford 1965; Rattray and Charnell 1966; Matsuno 1966) and also the first to be discovered in the atmosphere through an analysis of their equatorial meridional wind signals (Yanai 1963; Yanai and Maruyama 1966; Maruyama 1967, 1968; Maruyama and Yanai 1967). Following these initial studies, it was quickly established that MRGs were present from the surface up to at least 30 km in the stratosphere (Yanai et al. 1968; Yanai and Hayashi 1969; Yanai and Murakami 1970a,b; Nitta 1970). Although these disturbances were first studied as free (i.e., dry) modes, the latter papers included speculation that tropospheric MRGs might also be coupled to convection. This was confirmed as satellite irradiance data became more available (Chang 1970; Wallace 1971; Wallace and Chang 1972; Zangvil 1975). A historical review of these early MRG studies is provided in Takayabu et al. (2016), with summaries also given by Liebmann and Hendon (1990), Hendon and Liebmann (1991), Dunkerton (1993), and Dunkerton and Baldwin (1995).

Extensive work on MRGs since the 1970s has documented their role in modulating convection over the Pacific (Zangvil and Yanai 1980, 1981; Yanai and Lu 1983; Liebmann and Hendon 1990; Hendon and Liebmann 1991; Magaña and Yanai 1995; Dunkerton 1993; Dunkerton and Baldwin 1995; Yang et al. 2003, 2007a,b; Yokoyama and Takayabu 2012). There is ample evidence that MRGs can transform into easterly [also known as "tropical depression (TD) type"] waves over the western Pacific (Takayabu and Nitta 1993), some of which develop into tropical storms (Dickinson and Molinari 2002; Aiyyer and Molinari 2003; Frank and

Corresponding author address: George N. Kiladis, Physical Sciences Division, ESRL, 325 Broadway St., Boulder, CO 80305-3328.
E-mail: george.kiladis@noaa.gov

DOI: 10.1175/JAS-D-15-0230.1

Roundy 2006; Molinari et al. 2007; Chen and Huang 2009; Schreck et al. 2012). The role of vertically propagating MRG energy in forcing the quasi-biennial oscillation (QBO) is also well established (Lindzen and Holton 1968; Dunkerton 1997; Baldwin et al. 2001; Alexander et al. 2008b). Although they are fundamental components of tropical synoptic-scale variability, especially within the intertropical convergence zone (ITCZ) and the South Pacific convergence zone (SPCZ) in the west-central Pacific, we aim to show in this and a companion study (Dias and Kiladis 2016, hereafter Part II) that many aspects of MRGs have yet to be fully explored in both the troposphere and stratosphere.

The signature of convectively coupled MRGs is well defined in space–time spectra of satellite brightness temperature T_b and outgoing longwave radiation (Takayabu 1994; Wheeler and Kiladis 1999; Kiladis et al. 2009). The antisymmetric spectrum of tropical T_b about the equator is characterized by a continuum of power above the background with its peak closely following the dispersion curve of the theoretical $n = 0$ meridional mode from Matsuno's shallow water theory at an equivalent depth of around 25 m (Fig. 1a). Unlike other observed convectively coupled equatorial waves (CCEWs), whose spectral signatures are well separated into eastward and westward modes, there is a continuum of $n = 0$ power standing above the background that peaks near the lowest wavenumbers. Following Matsuno, the eastward-propagating signal is generally referred to as the $n = 0$ eastward inertio-gravity wave (EIG), whose dispersion relation asymptotically approaches that of a pure gravity wave at higher wavenumbers, with the westward branch called MRGs. Note that it is important to distinguish these modes from the broad spectrum of "internal" gravity waves that are not equatorially trapped (e.g., Bergman and Salby 1994; Dunkerton 1997; Baldwin et al. 2001; Alexander et al. 2008a; Kawatani et al. 2010), often referred to as simply "inertia–gravity" waves [see review by Fritts and Alexander (2003)].

Signals of the free-stratospheric MRGs originally observed by Yanai and Maruyama are also readily isolated by space–time spectral analysis (Ern et al. 2008; Lott et al. 2009; Alexander et al. 2008b; Alexander and Ortland 2010). For example, Fig. 1b is similar to Fig. 1a except it shows the spectrum of antisymmetric zonal wind at 50 hPa between 15°S and 15°N from ERA-Interim (ERAI) data. The spectral peak of these waves is centered on a much larger equivalent depth than for the T_b data, at around 120 m. Because of the impact of Doppler shifting by the zonal wind, the best fit to the dispersion curve is found by an adjustment to a westerly zonal wind of 3 m s^{-1}—an indication of the fact that MRG activity at this level is favored during the westerly phase of the QBO (Maruyama 1991; Dunkerton 1991; Alexander et al. 2008b; Alexander and Ortland 2010; Yang et al. 2011, 2012).

In contrast to decades of study and hundreds of published papers on dry and convectively coupled MRGs, the literature on $n = 0$ EIG waves is quite sparse. Free $n = 0$ and especially $n = 1$ EIG waves have been reported in the stratosphere and mesosphere (Mayr et al. 2003, 2004; Tindall et al. 2006a,b). Wheeler et al. (2000) and Kiladis et al. (2009) isolated the structure of $n = 0$ EIG waves and showed that their dynamical fields match their expected structures to some extent, although these differ to a greater degree from their theoretical structures than other CCEWs. Yang et al. (2003, 2007a) used a similar regression approach to isolate the structures of CCEWs, except that they fit the meridional wind structures to their expected scales using the parabolic cylinder functions associated with Matsuno's solutions as a basis [see also Gehne and Kleeman (2012)]. The $n = 0$ EIG structures in the Yang et al. (2007a) study (called EMRG waves in their Fig. 10a) do correspond well with that expected from theory; however, this is partly expected owing to the projection method used, which constrains the meridional wind structure to be symmetric about the equator and of a specified latitudinal scale owing to an assumed equatorial Rossby radius of 6°.

Despite strong spectral evidence of convectively coupled $n = 0$ EIG waves (herein "EIGs"), as opposed to the many studies of other CCEWs, apart from a case during July 1992 mentioned by Yang et al. (2003), to the authors' knowledge there are no observational case studies of these modes in the literature. Based on the evidence presented below and in Part II, we speculate that this may be due to the fact that EIGs often occur with accompanying MRG or other CCEW equatorial wave activity, and that while the spectrum in Fig. 1a in part represents propagating disturbances, there is also a tendency for nearly standing antisymmetric cloudiness about the equator associated with the lower-wavenumber spectral signals. In this paper we will discuss observed evidence for such propagating and standing components corresponding to MRGs and EIGs and confirm that while their stratospheric counterparts exist globally, convectively coupled MRG–EIG modes strongly favor the Pacific sector—the only region where a double ITCZ exists in the mean state (Fig. 2). Section 2 discusses the structure and propagation of $n = 0$ modes, section 3 outlines the data and methodology, and sections 4 and 5 present results of EOF and cross-spectral analyses. Variability of the modes is discussed in section 6, their association with extratropical forcing in section 7, and a summary and discussion is presented in section 8.

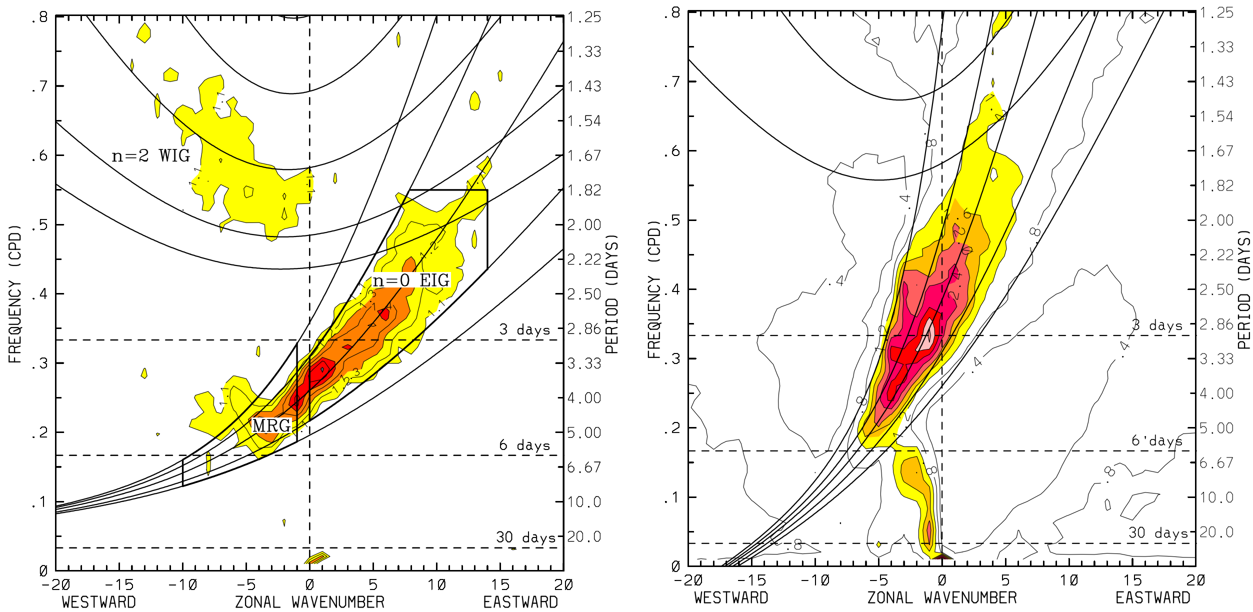

FIG. 1. Wavenumber–frequency power spectrum of the (left) antisymmetric component of CLAUS T_b for July 1983–June 2009, summed from 15°S to 15°N, plotted as the ratio between raw T_b power and the power in a smoothed red-noise background spectrum [see Wheeler and Kiladis (1999) for details]. Contour interval is 0.1, and contours and shading begin at 1.1. Dispersion curves for the $n = 2$ westward inertio-gravity waves (WIG), $n = 0$ EIGs, and MRGs are plotted for equivalent depths of 8, 12, 25, 50, and 90 m. (right) As in (left), but for the antisymmetric component of the zonal wind at 50 hPa summed from 15°S to 15°N, with equivalent depth curves of 25, 50, 120, 300, and 2000 m, Doppler shifted for a zonal wind of $+3\,\mathrm{m\,s^{-1}}$.

2. Structure of $n = 0$ MRG and EIG modes

Theoretical $n = 0$ MRGs and EIGs consist of antisymmetric pressure, zonal wind, and divergence fields about the equator and symmetric streamfunction and meridional wind fields (Fig. 3). The plots in Fig. 3 have been nondimensionalized so that the latitudinal scale is in terms of the equatorial Rossby radius:

$$R_e = \left(\frac{\sqrt{gh}}{\beta}\right)^{1/2},$$

where h is the equivalent depth, g is the gravitational constant, and β is the meridional gradient of the Coriolis parameter at the equator (Matsuno 1966). The divergence has been set to the same arbitrary value in all of the panels, and Fig. 3 is meant to represent low-level dynamical field with poleward flow into regions of convergence (blue).

In Fig. 3 it is obvious that MRGs are accompanied by a much stronger total circulation field than EIGs for a given divergence field. This difference will vary according to zonal wavenumber and equivalent depth for dimensional waves (Part II). MRGs are dominated by rotational flow with gyres centered on the equator (Fig. 3, left) while EIGs are primarily divergent with weak off-equatorial streamfunction signals (Fig. 3, bottom right). Both modes have cross-equatorial flow into regions of convergence, but in the case of EIGs the convergence is supplemented by zonal divergent flow, while in MRGs the zonal flow opposes the meridional convergence (Part II). The zonal wind, pressure, and divergence fields peak at $R_e = 1$ in both waves.

Looking back at Fig. 1a, the equivalent depth of the dispersion curve that best matches the $n = 0$ T_b spectral signal is around 25 m, similar to most of the other CCEWs identified using satellite data (Takayabu 1994; Wheeler and Kiladis 1999; Kiladis et al. 2009). In that case R_e would be around 7.5°, a value perhaps not coincidentally near the mean latitude of the ITCZ in the Northern Hemisphere (e.g., Holton et al. 1971; Chang 1973). Likewise, in Fig. 1b the implied 120-m equivalent depth yields an equatorial Rossby radius of around 11°, so we expect that the stratospheric MRG–EIG modes will have a larger meridional scale than those coupled to convection in the troposphere, as confirmed below.

3. Data and methodology

a. Datasets

We use the Cloud Archive User System (CLAUS) T_b data (Hodges et al. 2000), which has eight-times-daily global fields of T_b from July 1983 through June 2009,

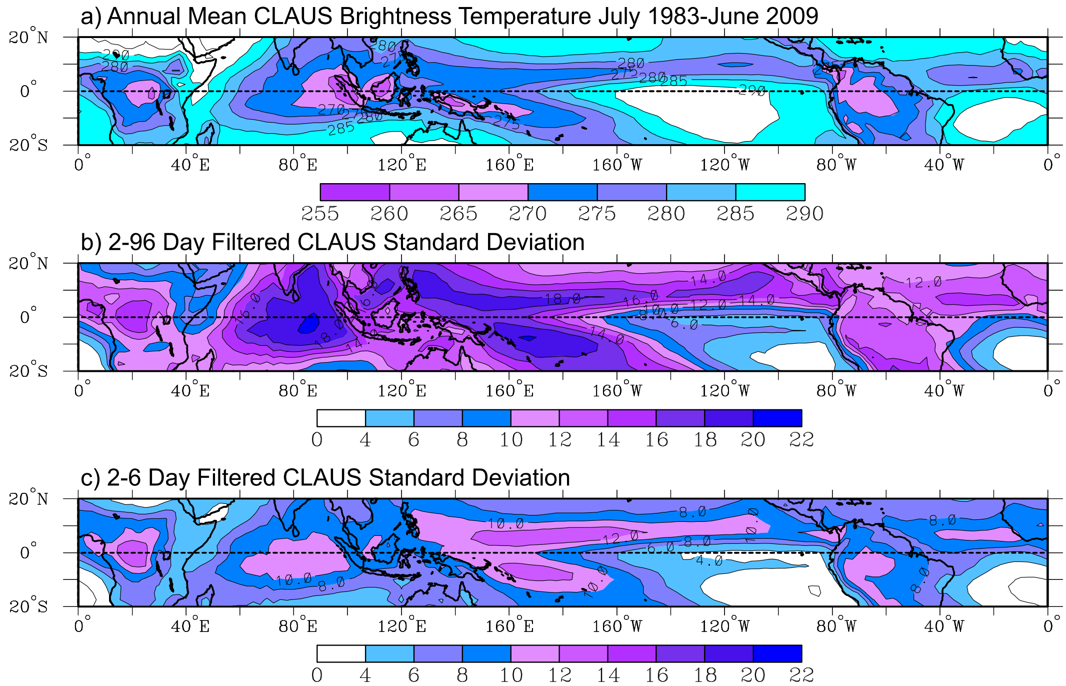

FIG. 2. (a) Annual-mean CLAUS T_b for the period July 1983–June 2009. Shading interval is 5 K. Standard deviation of four-times-daily (b) 2–96- and (c) 2–6-day-filtered CLAUS T_b for the entire 1983–2009 record. Shading interval is 2 K.

along with twice-daily interpolated outgoing longwave radiation (OLR) data (Liebmann and Smith 1996) and the TRMM 3B42 precipitation dataset (Huffman et al. 2007). MRG–EIG modes have relatively fast propagation speeds; therefore, the statistics for most of this study are obtained using the period that overlaps with the higher-temporal-resolution CLAUS data. OLR has also been used to extend these results and document wave activity back to 1974. The annual mean value of CLAUS T_b between 20°N and 20°S for the entire record is shown in Fig. 2a, which shows the familiar convective zones centered near the equator over land, the ITCZ between 5° and 10°N over the Pacific and Atlantic, and the SPCZ extending southeastward from the region of New Guinea.

For dynamical fields the ERAI dataset is used. Since the structures we are concerned with are relatively large scale, for computational convenience the ERAI, CLAUS T_b, and TRMM data have been interpolated to a regular 2.5° grid for our calculations, matching the spatial resolution of the OLR dataset. Virtually identical results have been obtained in tests using the higher-spatial-resolution products.

b. *Filtering and cross spectra*

Cross-spectral approaches have been used extensively as an objective means to document the existence, structure, and scale of equatorial waves (Yanai et al. 1968; Wallace and Chang 1969; Wallace 1971; Madden and Julian 1972). To obtain the cross spectra shown in this study, the data were first detrended and the first three harmonics of the seasonal cycle were removed, with tapering applied to 5% of the points at each end of the series. Spectral estimates were smoothed with a 301-point running average in frequency, and statistical significance was determined by a comparison of the coherence value distributions with those obtained through Monte Carlo simulations of cross spectra by generating a background obtained from running one time series backward, preserving its autocorrelation, calculating its coherence, then adding the 1000 estimates of the coherence generated by random-Gaussian-noise time series. Several parametric methods were also tested (e.g., Blackman and Tukey 1958), all yielding similar results. In the cross-spectra plots below, all of the regions of shaded coherence are significant at better than the 99% level.

Various methodologies have been used in the past to obtain the statistical horizontal and vertical structure of MRGs–EIGs from gridded analyses, typically using filtered data as a basis to isolate scales of interest. Here we utilize filters based on the Fourier space–time decomposition described in Wheeler and Kiladis (1999), where we include all wavenumbers for temporal

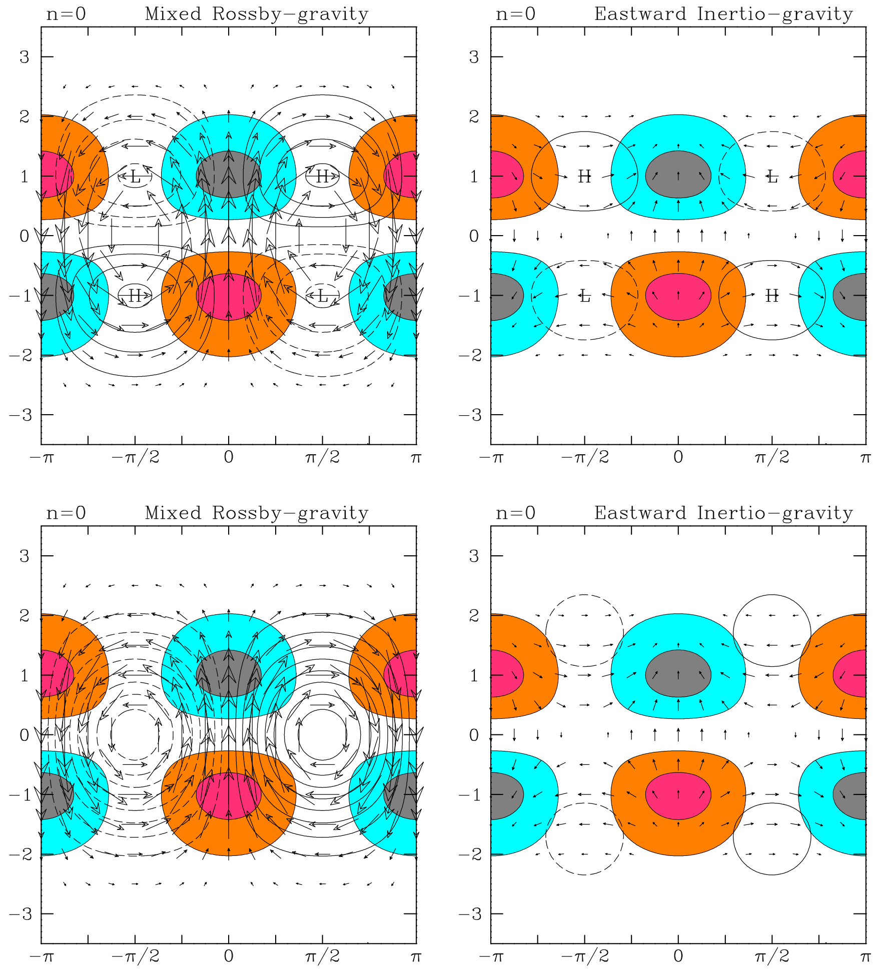

FIG. 3. Theoretical structure of the $n = 0$ MRG and EIG modes. (top) The geopotential (contours; dashed negative), divergence (shading; blue negative), and vector winds are shown for the MRG and EIG, respectively, with (bottom) the streamfunction displayed as contours. The divergence has been scaled to the same dimensionless value in all panels, with the same arbitrary geopotential contour interval used in (top). The streamfunction interval in (bottom right) is one-half that used in (bottom left).

filtering. We also utilize westward- or eastward-only filters that retain either negative or positive wavenumbers, respectively, excluding wavenumber 0. For comparison purposes we display the four-times-daily standard deviation of 2–96-day-filtered T_b in Fig. 2b. This filter effectively removes the diurnal and seasonal cycles, along with interannual variability, and shows that the regions of largest intraseasonal and synoptic-scale variability generally coincide with regions of deepest mean convection implied in Fig. 2a.

As seen in Fig. 1, most of the power above the background of the tropospheric and stratospheric $n = 0$ modes lies within 2–6 days and this period brackets the filter bands we use for the EOF analyses in this study. Figure 2c shows that the 2–6-day-filtered standard deviation in fact accounts for the bulk of the subseasonal wave activity over many regions and for more than 70% of the signal seen in Fig. 2b over the Pacific. In particular, such synoptic-scale activity accounts for most of the variability within the ITCZ and SPCZ, far exceeding that of the MJO, for instance. Also included within the 2–6-day band are easterly waves or TD-type disturbances (Takayabu and Nitta 1993; Wheeler and Kiladis 1999) but it will be shown that these are well separated from MRG–EIG disturbances by the EOF approach used here.

c. *EOF approach*

As pointed out by Dunkerton and Baldwin (1995), the use of point correlations as an analysis tool is compromised when representing the statistical structures of waves from gridded analyses because of the relatively small ''coherence length'' of fluctuations when all scales of motion are included. When linear dynamics is dominant, EOFs can be a useful alternative if used judiciously and with an eye toward the underlying dynamics (e.g., Monahan et al. 2009).

EOFs are calculated using the covariance matrix of filtered T_b within 20°S–20°N for both global domains and domains localized in longitude. The dynamical fields associated with each EOF are obtained by projecting unfiltered ERAI data at each grid point onto the associated principal component (PC) time series. In the following analysis, streamfunction and statistically significant T_b fields will be shown, with associated wind perturbations displayed only if either the zonal or meridional wind is significant at the 95% level, after taking into account the autocorrelation in each field as described by Livezey and Chen (1983).

4. EOF results

We first demonstrate the ability of spatial EOFs to isolate the stratospheric MRG modes first detected by Yanai and Maruyama (1966). Figure 4 shows the first four EOFs of 2–6-day meridional wind at 50 hPa for the entire tropical belt between 20°S and 20°N. As with the rest of the plots in this paper, these patterns have been scaled to a +2 standard deviation perturbation in their respective PCs—a typical amplitude for strong events. The EOFs isolate gyres centered on the equator having the structure of MRG waves in Fig. 1. The first two EOFs form a quadrature pair and are correlated at 0.76 with PC1 leading, which from Figs. 4a and 4b implies westward propagation. Similarly, the third- and fourth-EOF PCs are correlated at 0.67, with the fourth leading, also implying westward-propagating MRGs. Together the first two EOFs explain nearly 15% and the third and fourth explain 13% of the filtered variance. Results using the 2–6-day vorticity or the antisymmetric components of the zonal wind, geopotential, or temperature are quite similar (not shown).

The EOF pairs in Figs. 4a–d represent two distinct scales of stratospheric MRGs. The gyres in Figs. 4a and 4b are zonal wavenumber-4 disturbances that propagate westward at around 30 m s^{-1}, giving a mean period of around 4 days, although this varies depending on season and the phase of the QBO. In Figs. 4a and 4b, this leading pair is localized to the sector extending from the Americas, across the Atlantic into Africa. The next EOF pair represents a zonal wavenumber-3 pattern with its loading more zonally distributed but also with a minimum over the Pacific. These waves propagate at a much faster phase speed of around 45 m s^{-1}, yielding a period close to 3.5 days. Higher-mode pairs out to at least EOFs 7 and 8 account for MRG activity over other sectors. One point of critical relevance to our arguments below is that westward-propagating MRGs can be isolated in the stratosphere by EOF analysis of 2–6-day-filtered data, without having to filter explicitly for westward propagation.

Although stratospheric waves are not the primary focus of this study, some points about these modes are relevant here. While there are statistically significant correlations between the circulations shown in Fig. 4 and T_b, their amplitudes are small (<2°K). This agrees with results of Hendon and Wheeler (2008), who also showed weak but significant coherence between antisymmetric zonal winds at 50 hPa and OLR. Interestingly, despite the weak convective coupling, circulations that are significantly correlated with these EOFs do extend down through the troposphere to the surface, although these are also relatively small amplitude (not shown). Consistent with past results such as Maruyama (1991), Dunkerton (1991), Alexander et al. (2008b), and Yang et al. (2011, 2012), there is a large modulation of the activity of these waves by the QBO—a topic that will be pursued in a future study.

Next, we adopt the same procedure to isolate the structure of convectively coupled MRG–EIG modes, except that 2–6-day-filtered brightness temperature T_{b26} from 20°S to 20°N was used as an EOF basis. In this case, the analysis yields leading EOFs with maximum T_b amplitude over the Pacific, collocated with the maximum ITCZ and SPCZ variance in that frequency band in Fig. 2c. This analysis was repeated by season, and very similar Pacific EOFs were obtained, except that during December–February (DJF) and March–May (MAM) they occupy the third and fourth modes, with the leading modes instead collocated with the variance peak over Africa in Fig. 2c. However, these modes display eastward propagation and are associated with very weak meridional wind signals, indicative of Kelvin wave activity. To concentrate on the Pacific variability, we discuss here the results of the annual EOF analysis of T_{b26} for the domain 20°S–20°N, 120°E–120°W, where MRG–EIG activity is dominant.

Figure 5 shows the first two EOFs (shading) and also the associated 850-hPa circulation pattern obtained by regression onto the PCs. Individual seasonal EOFs using the same domain are nearly identical to these annual results and with the corresponding EOFs of year-round global data for 20°S–20°N as well as to EOFs calculated from combined MRG–EIG filtered data using the filtering boxes shown in Fig. 1a, with correlations between respective PCs in excess of 0.75 in all cases. The seasonal dependence of the modes will be discussed more fully below and in Part II.

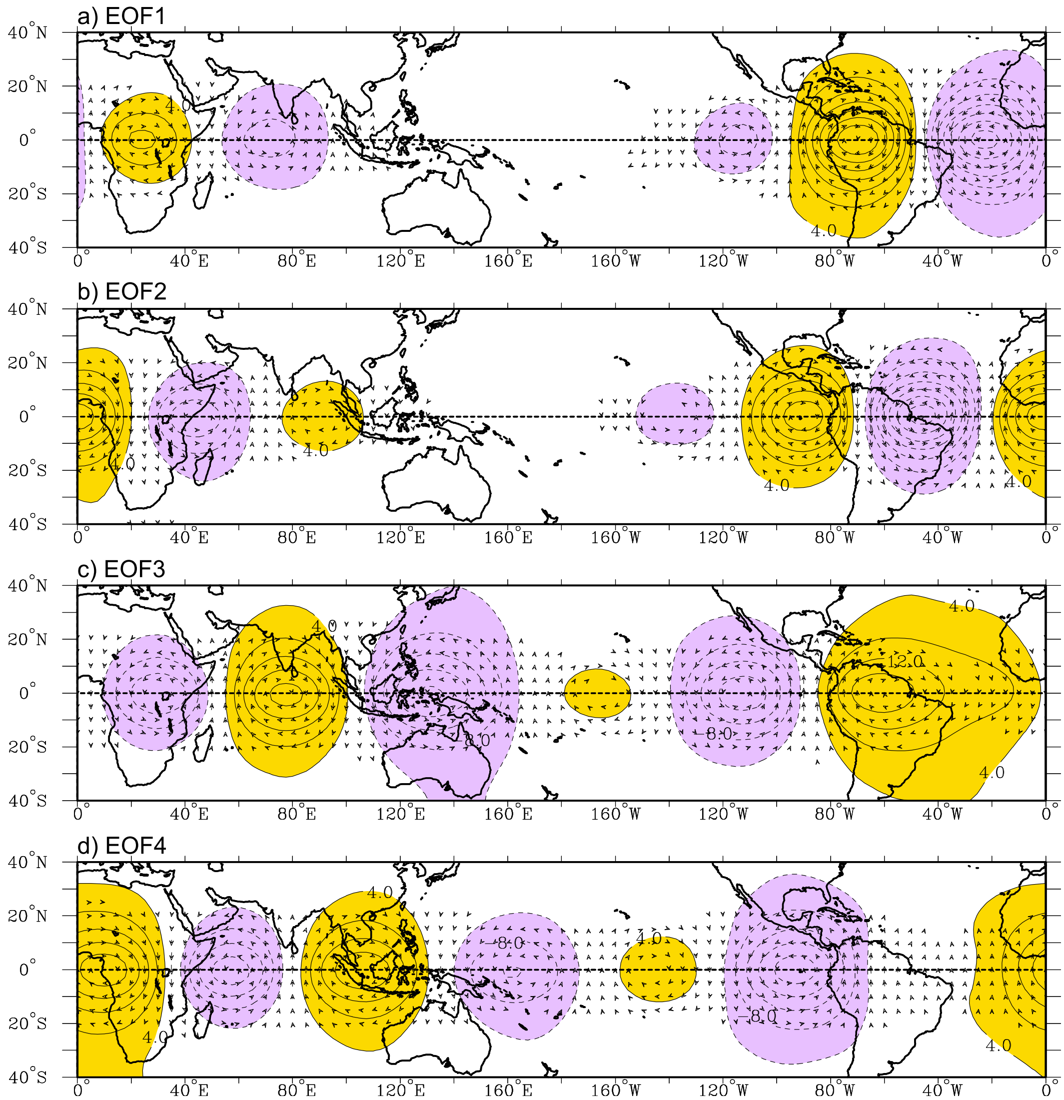

FIG. 4. The 50-hPa streamfunction and wind regressed onto four-times-daily 1979–2012 PCs corresponding to (a) EOF1, (b) EOF2, (c) EOF3, and (d) EOF 4 of the 2–6-day-filtered 50-hPa meridional wind between 20°S and 20°N. All fields are scaled to a +2 standard deviation PC perturbation. Streamfunction contour interval is $4 \times 10^5\ m^2\ s^{-1}$, with solid contours and yellow shading corresponding to positive perturbations. Vector winds are shown if either the zonal or meridional wind is statistically significant at the 95% level. The largest wind vectors correspond to speeds of around $3\ m\ s^{-1}$.

Earlier investigations such as Hendon and Liebmann (1991) and Dunkerton (1993) used antisymmetric OLR to isolate MRGs, and although we did not use this decomposition as a basis in our EOF calculations, the two leading modes still show an out-of-phase fluctuation in T_b between the ITCZ and SPCZ in Fig. 5 [the overwhelming tendency for such out-of-phase relationships in T_b at these frequencies in the central Pacific was first shown by Wallace (1971)]. MRG-like circulations accompany these convective signals, with negative T_b or enhanced convection consistent with the theoretical patterns of low-level convergence in Fig. 3a. EOF1 and EOF2 explain 3.4% and 3.0% of the variance, respectively, which is marginal in terms of their separation as independent modes by the criteria of North et al. (1982). These EOFs do represent a propagating pair but only at a correlation of 0.19 with the first mode leading (Part II). While this would result in a westward-propagating cloud field, the zonal scales of the T_b signals also differ significantly. Thus, we will initially analyze these EOFs separately.

In Fig. 6 we lag regress the total T_b, 850-hPa streamfunction and wind on the PC1 time series of EOF1 in Fig. 5a. A striking feature of the behavior of T_b in Fig. 6 is that its propagation is primarily in the meridional, rather

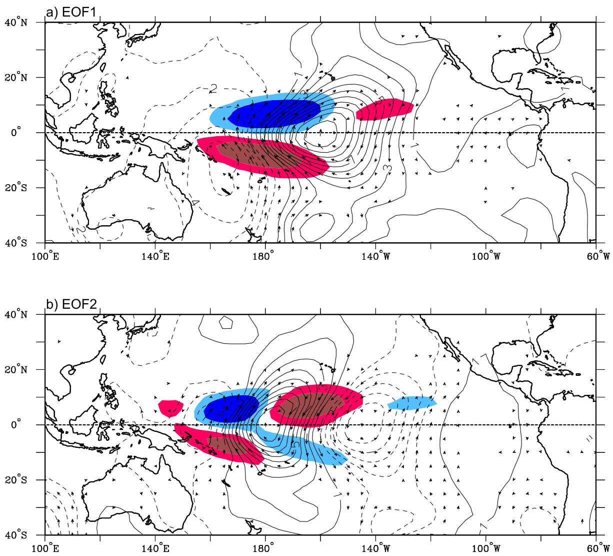

FIG. 5. As in Fig. 4, but for (a) EOF1 and (b) EOF2 of T_{b26} between 20°S and 20°N, 120°E and 120°W for the period 1983–2009, along with the regressed streamfunction at 850 hPa. The shading for T_b starts at ±2 (lighter colors) and ±6 K (darker colors), with negative values in blue. Streamfunction contour interval is $1 \times 10^5\ \mathrm{m^2\,s^{-1}}$. The largest wind vectors correspond to speeds of around $1.5\ \mathrm{m\,s^{-1}}$.

than zonal, direction. In contrast, MRG-like circulations in the 850-hPa streamfunction fields are propagating westward through the region of zonally standing convective signals. The zonally standing versus propagating nature of these signals is brought out by Fig. 7, which shows a time–longitude plot of T_b at 7.5°N along with the rotational component of the meridional wind on the equator for 25 days surrounding the peak in PC1. Fluctuations in the rotational meridional wind propagate westward at $25\ \mathrm{m\,s^{-1}}$—a nearly identical phase speed as the leading-mode stratospheric MRGs described above and the tropospheric MRGs reviewed in section 1. If instead the divergent meridional wind is plotted, this shows a dominant zonally standing component, and other fields related to the mass circulation such as the horizontal divergence and vertical motion also display similar behavior consistent with T_b in Fig. 6 (not shown). Also tested was whether the T_b signals truly represent convection rather than simply high-cloudiness perturbations that might be advected by the upper-tropospheric flow. This was verified in two ways: by calculating EOFs using four-times-daily TRMM 3B42 precipitation data and also by projecting the TRMM data onto the PCs obtained above from T_b data for the overlapping period (1998–2009). These results retain all of the same antisymmetric, zonally standing, but poleward propagating characteristics as the T_b data show (not shown).

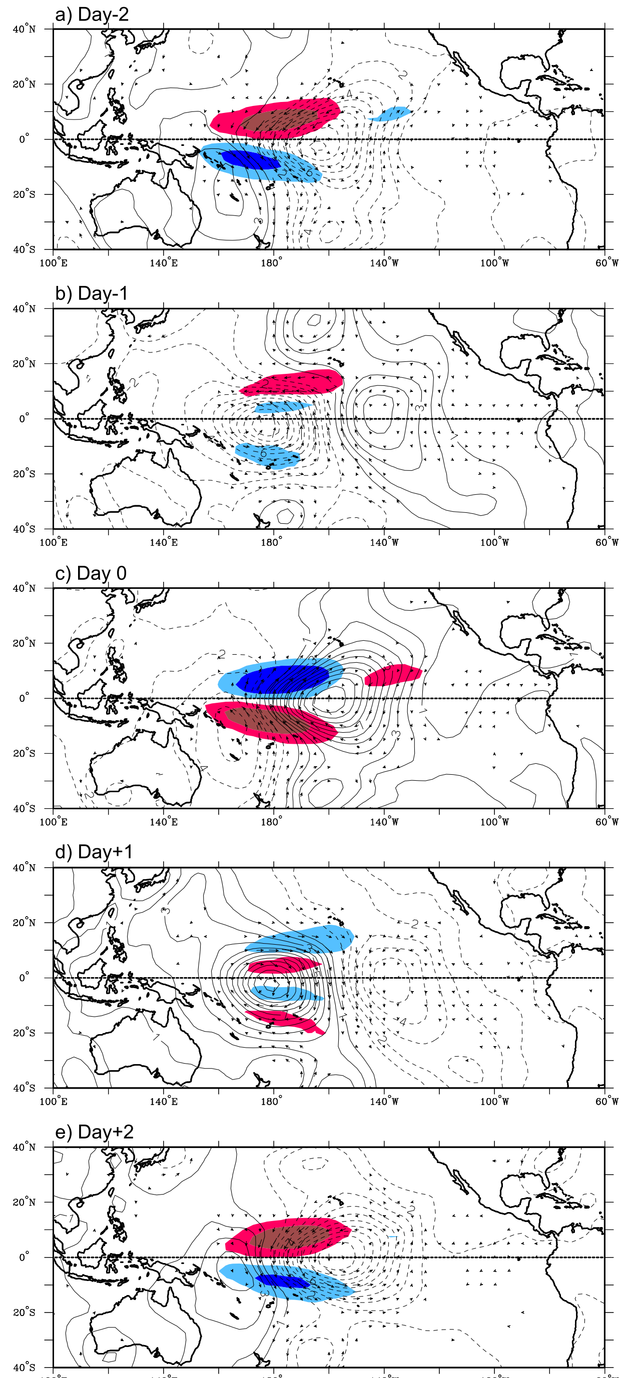

FIG. 6. As in Fig. 5, but for T_{b26} EOF1 from day −2 through day +2.

Standing antisymmetric signals of cloudiness between the ITCZ and SPCZ on the time scale of $n = 0$ modes have been reported in the literature, but this observation has not received any recent attention. In his comprehensive spectral study of radiosonde and T_b data over the Pacific, Wallace (1971) remarked on the fact that "…the $n = 0$ mode is not evident in the brightness data

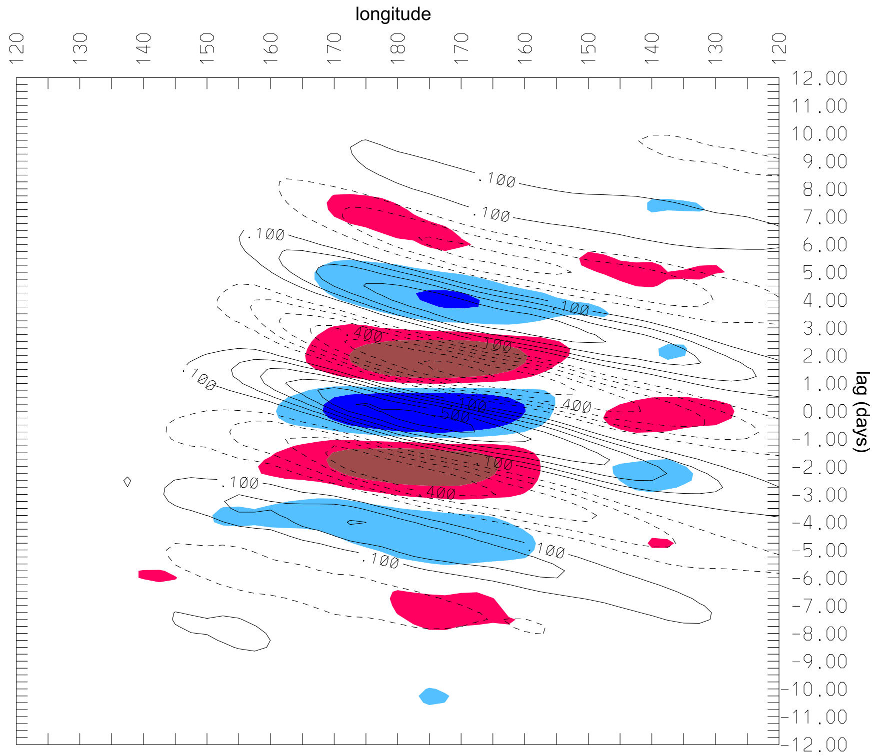

FIG. 7. Time–longitude diagram of T_b at 7.5°N and the rotational component of the meridional wind on the equator regressed onto the four-times-daily 1983–2009 PC of T_{b26} EOF1. Shading for T_b starts at ±2 (lighter colors) and ±6 K (darker colors), with negative values in blue. The contour interval for the wind is 0.1 m s^{-1}.

as a zonally propagating wave. It may be more appropriate to view it as a standing oscillation confined to the central Pacific.'' Following up on this observation, Holton (1972) showed that westward-propagating MRG circulations with upward and eastward group velocity could be produced in a linearized primitive equation model forced by standing antisymmetric heating with a period of 5 days. Hendon and Liebmann (1991) speculated that standing 5-day convective patterns might have been peculiar to the single season that Wallace analyzed, motivated by the fact that they isolated a strong westward-propagating signal using bandpass-filtered antisymmetric OLR for 3.5–6.5-day periods during October–November. Takayabu and Nitta (1993) also produced a zonally standing T_b pattern by lag correlating 2.5–10-day-filtered T_b with itself at the base point 5.5°N, 179.5°E. In fact, their T_b pattern does also display distinct poleward propagation in both hemispheres (their Fig. 5a), although this point was not emphasized in their study.

We can reproduce the westward-propagating point correlation result of Hendon and Liebmann (1991) as in their time–longitude diagrams using identically filtered OLR or T_b, but when 2–6- or 2–10-day-filtered data are used (either symmetric or antisymmetric), the signal is dominated by a zonally standing pattern analogous to that in Fig. 7. The difference between these results holds during all times of the year, so it is not just a seasonal dependence. As shown by Part II, one source of this discrepancy lies in the fact that the 3.5-day cutoff used by Hendon and Liebmann (1991) excludes the bulk of EIG power seen in Fig. 1a. Even point correlations derived from 3.5–6.5-day antisymmetric OLR or T_b data still show much stronger meridional than zonal propagation as in Fig. 6 when mapped at lag, while the associated circulations still propagate westward (not shown). Hints of this meridional propagation are actually seen in plots of Liebmann and Hendon (1990) and Hendon and Liebmann (1991) (e.g., their Figs. 11 and 8, respectively); however, a focus on time–longitude diagrams at one latitude in those studies and in Dunkerton and Baldwin (1995) seems to have precluded a more thorough documentation of this tendency.

The circulations in Fig. 6 are somewhat distorted, more zonally elongated versions of the MRG structures generally pictured in the literature (e.g., Liebmann and Hendon 1990; Hendon and Liebmann 1991; Dunkerton and Baldwin 1995; Wheeler et al. 2000; Kiladis et al. 2009), so a legitimate question arises as to whether these structures are a statistical artifact of the EOF approach. This was tested by performing the same EOF analysis on westward-propagating (excluding wave 0) 2–6-day-filtered brightness temperature T^{w}_{b26}, and that result is shown in Fig. 8. As with the stratospheric MRG results in Fig. 4, this time the procedure yields a family of propagating mode pairs, with the first two pairs correlated at 0.91 and the second two at 0.89. These pairs explain a combined variance of 9.3% and 6.3%, respectively.

The first pair, as represented by EOF1 (Fig. 8a), recovers the structures discussed in previous tropospheric MRG studies, including the poleward and eastward tilts of the T_b signals that are only weakly present in the zonally standing disturbances of Fig. 5. A similar but less exaggerated anisotropy in the streamfunction contours was also seen by Liebmann and Hendon (1990), Takayabu and Nitta (1993) Dunkerton and Baldwin (1995), Kiladis et al. (2009), and Roundy and Janiga (2012). This EOF displays the westward propagation of the T_b signal in lockstep with their associated circulations at around 22 m s^{-1}, without any evidence of meridional propagation (not shown). The second pair, as shown by EOF3 (Fig. 8b) represents the transition of MRG to TD disturbances that frequently occurs over the western Pacific (Liebmann and Hendon 1990; Takayabu and Nitta 1993; Numaguti 1995; Dickinson and Molinari 2002; Straub and Kiladis 2003b; Kiladis et al. 2009). This transition is considered to be due in part to deformation and the accumulation of wave energy brought on by the convergence of the basic-state zonal westerly flow over the region (Sobel and Bretherton 1999; Kuo et al. 2001; Aiyyer and Molinari 2003; Chen and Huang 2009).

The fact that zonally standing signals constitute the leading modes in the T_b fields in Figs. 6 and 7 means that these signals are indeed dominant, since if westward propagation was preferred, these would have shown up as the leading EOF modes of 2–6-day-filtered data as in the case of the stratospheric EOFs of Fig. 4. This point will also be demonstrated using synthetic data by Part II. While the modes represented by Fig. 8 are not completely independent of those shown in Fig. 5a, with correlations running in the 0.58 range between the respective PC pairs, we demonstrate below and in Part II that while they often do occur independently, the zonally standing EOF results in Figs. 6 and 7 are dominant.

5. Cross-spectral results

Cross-spectral analysis between various dynamical fields and OLR has been particularly effective at isolating the structure of convectively coupled MRGs (e.g., Yanai et al. 1968; Wallace 1971; Chang and Miller 1977; Zangvil and Yanai 1980, 1981; Liebmann and Hendon 1990; Hendon and Liebmann 1991; Dunkerton 1993). Based on analyses of global data, the latter three studies argued that convectively coupled MRG activity is primarily confined to the central Pacific near the date line, with dry MRG circulations still prevalent over the east Pacific and Atlantic. More recent work using spatially windowed space–time spectra also indicates that convectively coupled MRG–EIG activity peaks over the Pacific (Dias and Kiladis 2014), although completely localizing their signals is not possible using their methodology. Maps of MRG–EIG T_b variance also show maxima over the Pacific with some variability extending into other ocean basins (Wheeler and Kiladis 1999; Roundy and Frank 2004; Kiladis et al. 2009), but in those cases it is not clear how much of the signal is truly indicative of the filtered mode versus the potential for misrepresentation by the inclusion of "background" variability. In this section we employ cross-spectral approaches using dynamical fields, along with T_b, to better nail down the geographic extent of the signals due to MRG–EIG modes in the troposphere and stratosphere.

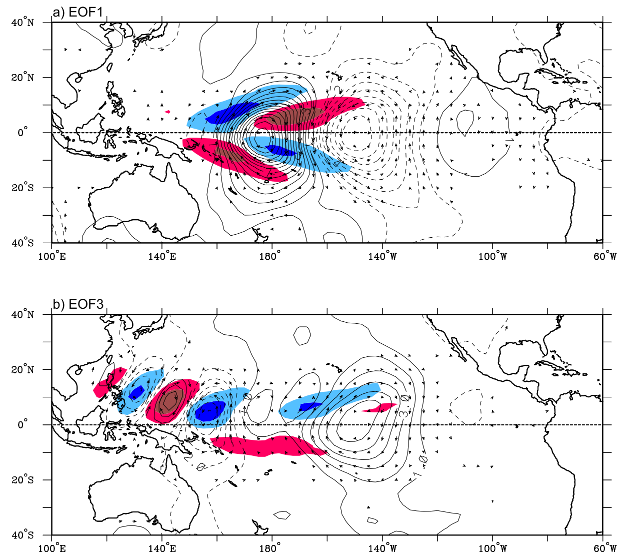

FIG. 8. As in Fig. 5, but for (a) EOF1 and (b) EOF3 of T^{w}_{b26}.

Figure 9a shows the raw spectral power of the meridional wind on the equator at 50 hPa plotted at each longitude for frequencies between 0.011 and 0.5 cycles per day (i.e., periods from 90 to 2 days). This spectrum is quite remarkable in that, even though we have only removed a trend without the "prefiltering" that has often been used in early studies (e.g., Yanai et al. 1968), it shows a very pronounced peak at 3–5-day periods present at all longitudes, without any sign of reddening

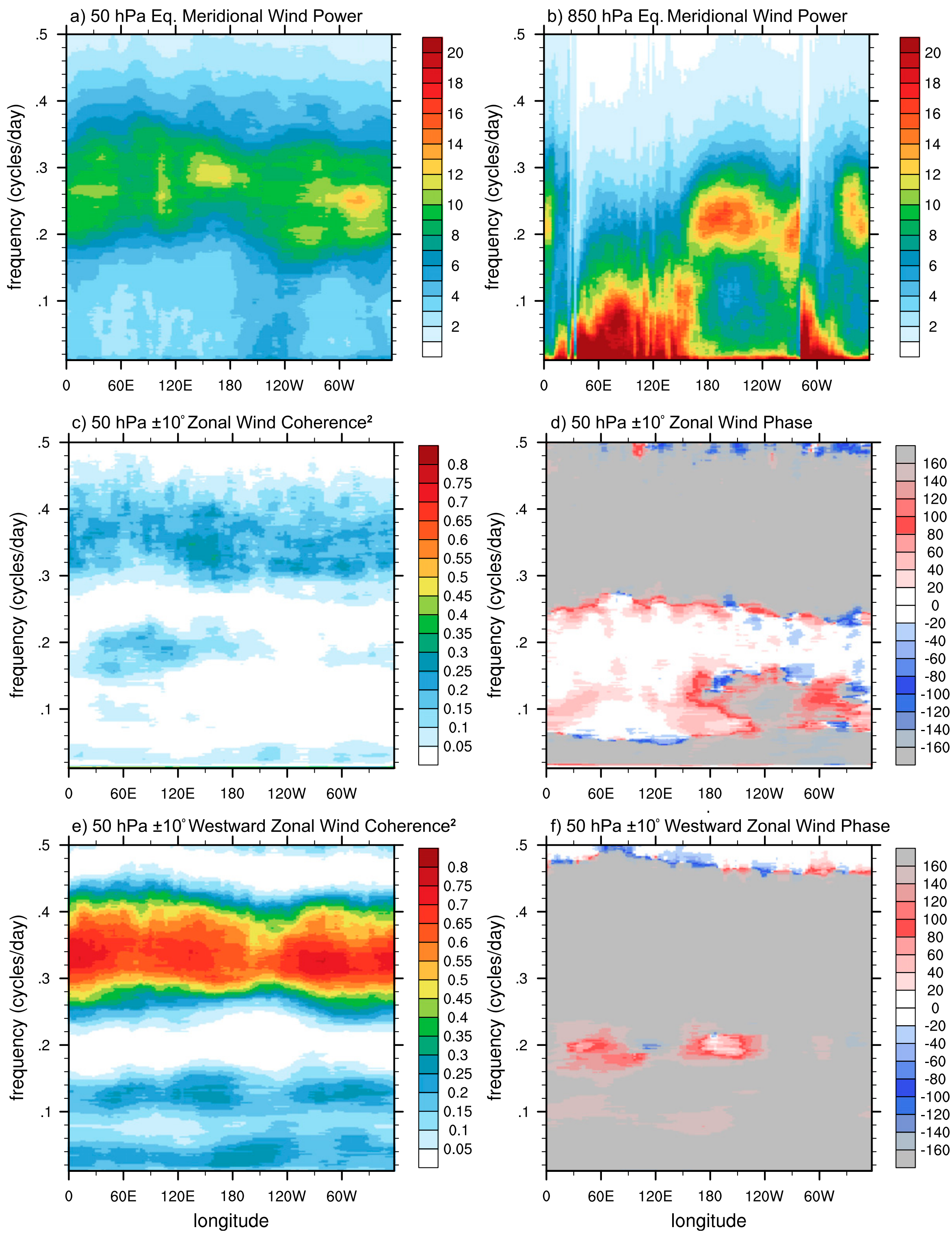

FIG. 9. Spectral power by frequency and longitude of ERAI equatorial meridional wind at (a) 50 and (b) 850 hPa. Cross-spectral (c) coherence squared and (d) phase between 50-hPa zonal wind at 10°N and 10°S. Cross-spectral (e) coherence squared and (f) phase between westward-only-filtered 50-hPa zonal wind at 10°N and 10°S. Shading in (d) and (f) represents phase, with white showing in-phase and gray showing out-of-phase coherence and reddish shading denoting 10°N leading by the phase angle on the scale. The entire record from 1979 through 2012 was used to calculate all of the plots.

at lower frequencies typically seen in most spectra of observed parameters in the atmosphere. Past spectral studies (Yanai et al. 1968; Yanai and Hayashi 1969; Dunkerton 1993) as well as the EOF results of Fig. 4 leave little doubt that this signal is dominated by MRG activity. The equivalent plot for 850-hPa meridional wind in Fig. 9b shows two strong spectral peaks representing activity between 3 and 4 days, but these are only evident over the central and east Pacific and Atlantic, giving way to a more typical red spectrum at other longitudes. The implications of this spectral power distribution will be discussed further below.

In Figs. 9c and 9d, the squared coherence and phase between 50-hPa zonal wind at 10°N and 10°S is plotted. Tests show that using a latitude of 10° maximizes the coherence, consistent with the 11° theoretical equatorial Rossby radius for a 120-m equivalent depth discussed in section 2. There are three main bands of statistically significant coherence in Fig. 9c, one of which is in phase at around 0.2 cycles per day centered over the Indian Ocean and western Pacific. This peak can be associated with ''fast'' stratospheric Kelvin waves (Ern et al. 2008; Alexander et al. 2008b; Alexander and Ortland 2010; Yang et al. 2011; Maury and Lott 2014), the structure of which is readily isolated by applying the EOF technique described above to appropriately filtered data (not shown). The other two peaks in Fig. 9c are out of phase at between 0.3 and 0.4 cycles per day and at less than 0.05 cycles per day, both of which extend across all longitudes. Regions of high in-phase coherence would be expected for any large-scale propagating features with a symmetric structure such as Kelvin waves. Out-of-phase relationships, however, are likely generated by antisymmetric wave structures.

To illustrate this point further, cross-spectral results for westward-propagating 50-hPa zonal wind between 10°N and 10°S are shown in Figs. 9e and 9f. The westward coherence squared in Fig. 9e is extremely high and out of phase, exceeding 0.65 globally and centered on waves with a period of 3 days (~0.33 cycles per day), with minimum values over the central Pacific, consistent with the leading MRG EOF patterns shown in Fig. 4. The out-of-phase westward signals centered at 0.12 cycles per day and the lowest-frequency peak at the bottom of Figs. 9e and 9c are likely due to the free external zonal wavenumber-1 and -2 Rossby modes with periods of around 7 and 28 days, respectively, which have antisymmetric zonal wind structures [e.g., the 2–2 and 1–4 modes from Madden (2007)], the spectral peaks of which can also be seen in Fig. 1b. As expected the 0.2 cycles per day ''fast'' Kelvin peak in Figs. 9c and 9d is absent in Figs. 9e and 9f.

We now apply the same procedure to T_b in Fig. 10. For these spectra the maximum coherence is between 7.5° on either side of the equator, in agreement with the smaller equivalent depth and equatorial Rossby radius of convectively coupled modes discussed in section 2. Unfiltered T_b coherence squared and its phase are shown in Figs. 10a and 10b. In this case coherence is much lower than for zonal wind in the stratosphere in Figs. 9c and 9e (note change in scale), with the most prominent signal out of phase and spanning a broad frequency range corresponding to periods of between 3 and 5 days. The maximum covariance lies within a 60° region centered just west of the date line and, so, likely represents at least in part the antisymmetric fluctuations represented by the T_{b26} EOFs in Fig. 4. Weaker out-of-phase secondary peaks in the same frequency band are also seen over Africa and South America just west of 30°E and 60°W, respectively. When westward-only T_b is used (Figs. 10c,d), the peak coherence becomes more concentrated at around 0.22 cycles per day, corresponding to the 4.5-day period of observed convectively coupled MRG waves in Figs. 8a and 8b, so this signal likely represents the antisymmetric T_b fluctuations associated with those waves. Likewise, eastward-only T_b spectra (Figs. 10e,f) also show out-of-phase peaks over the same region of the Pacific, along with a smaller peak over Africa, but in the higher frequency range of the EIG spectral peak in Fig. 1a. It therefore appears that the cross spectra are isolating the signal of convectively coupled MRGs and EIGs and, moreover, the central Pacific is the primary region where there is an antisymmetric T_b signal associated with these waves. This raises the question as to whether the double ITCZ in Fig. 2 is the one region that favors the dominance of antisymmetric convective signals, or whether such signals can still exist in other regions with ITCZ convection more centered on the equator.

To test whether convectively coupled MRG–EIG convective signals could be present in one hemisphere only, we examined cross spectra between off-equatorial T_b and wind at all 37 available levels in ERAI from the surface to 1 hPa. The most significant results were obtained using 850-hPa meridional wind at the equator and T_b at 7.5°N, as shown in Figs. 11a and 11b. The strongest signals show out-of-phase relationships, as would be expected from Fig. 3 and also Figs. 5 and 8, where equatorial southerlies at 850 hPa are accompanied by negative T_b anomalies in the ITCZ and positive anomalies in the SPCZ. Highest coherence is again seen over the central Pacific for 3–5-day periods, with secondary peaks along the coast of South America (near 90°W) and the Atlantic. Similar results were obtained using T_b at 7.5°S (not shown). Consistent with analyses by Liebmann and Hendon (1990), Hendon and Liebmann (1991), Numaguti (1995), and Dunkerton and Baldwin

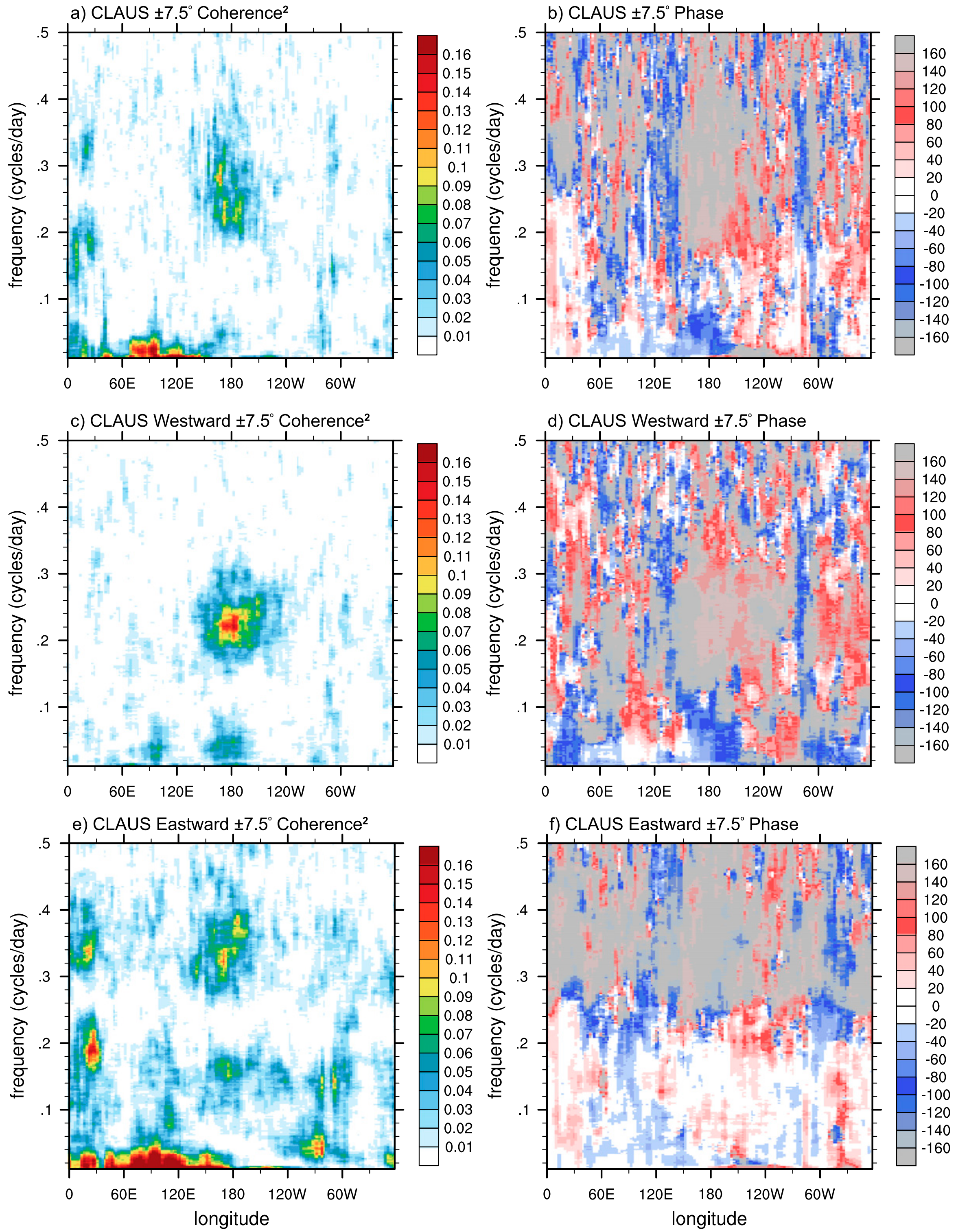

FIG. 10. As in Fig. 9, but for coherence squared and phase between (a),(b) CLAUS T_b at 7.5°N and 7.5°S, (c),(d) westward-only-filtered CLAUS T_b at 7.5°N and 7.5°S, and (e),(f) eastward-only-filtered CLAUS T_b at 7.5°N and 7.5°S. The entire record from 1983 through 2009 was used to calculate all of the plots.

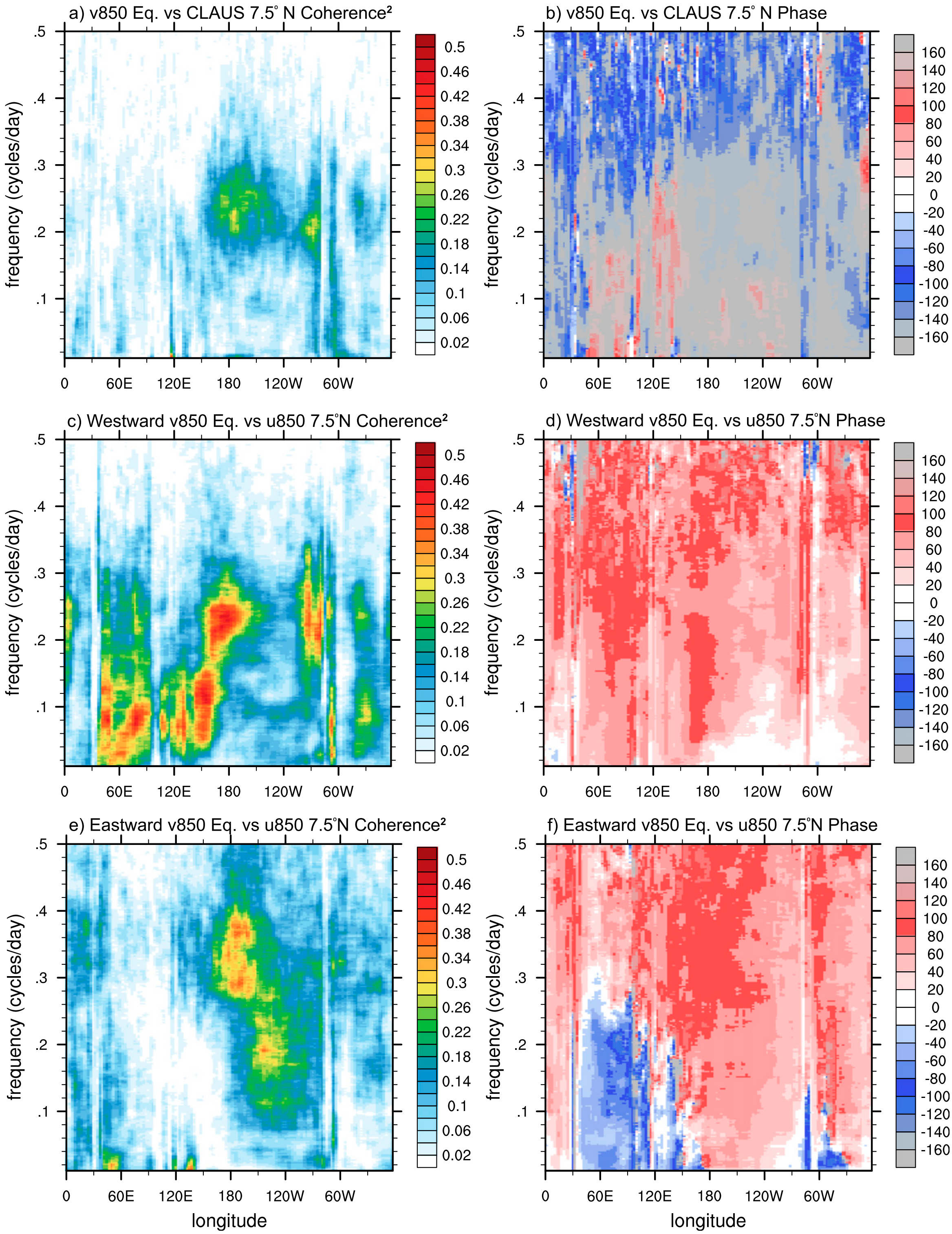

FIG. 11. As in Fig. 9, but for coherence squared and phase between (a),(b) 850-hPa meridional wind at the equator and CLAUS T_b at 7.5°N, (c),(d) westward-only 850-hPa meridional wind at the equator and zonal wind at 7.5°N, and (e),(f) eastward-only 850-hPa meridional wind at the equator and zonal wind at 7.5°N.

(1995), coherence between T_b and circulation drops off rapidly above 500 hPa, although there is some evidence for convective coupling with lower-frequency equatorial eddies in the mid- to upper troposphere over a range of longitudes in the Indian sector (not shown).

We also attempted to isolate MRG–EIG circulations by calculating the coherence between equatorial meridional and off-equatorial zonal wind. For example, in Figs. 11c and 11d we show the coherence and phase between 850-hPa westward-propagating meridional wind on the equator and westward-propagating zonal wind at 7.5°N. At nearly all longitudes and frequencies, the phase relationship is such that the meridional wind leads the zonal wind by 1/4 cycle (i.e., close to +90° in Fig. 11b), indicative of westward propagating eddies centered on the equator (Fig. 3, left panels). Once again, coherence in the 3–5-day period is largest centered on the date line; however, other regions of coherence are also seen over the easternmost Pacific (90°W) and Atlantic (30°W). Figures 11c and 11d also provide evidence for lower-tropospheric equatorial eddies over the western Pacific, Indian Ocean, and Atlantic that are not visible in Figs. 11a and 11b and so are not strongly coupled to convection. In particular, MRG-like circulations have been reported over the Indian Ocean (Yasunaga et al. 2010; Muraleedharan et al. 2015; Chen et al. 2015), although these are often identified as off-equatorial eddies (e.g., Kerns and Chen 2014). Spectra similar to those in Fig. 11 for other levels reveal equatorial eddies prevalent in the mid- to upper troposphere, especially over the Indian sector, although these have a much broader range of frequencies than those over the central Pacific, extending to periods beyond 10 days (not shown).

Figures 11e and 11f are similar plots except for 850-hPa eastward-only meridional wind on the equator and eastward zonal wind at 7.5°N. As with signals associated with eastward T_b in Figs. 10e and 10f the coherence is largest near the date line and over Africa in the higher frequency range of EIGs, with a phasing of +90° that would be consistent with eastward-propagating EIG circulations in the right panels of Fig. 3. There is also some signal over the Atlantic, along with a lower-frequency quadrature peak extending down to 0.1 cycles per day over the eastern Pacific. The nature of this eastward 5–10-day peak is not clear, although we speculate that it might be related to equatorial eddies excited by extratropical wave activity propagating into the equatorial region of the east Pacific (e.g., Kiladis 1998; Yang et al. 2007b), to be discussed further below.

A similar approach was systematically applied to raw and eastward- or westward-filtered T_b, along with various combinations of wind data for all levels from the surface to the midstratosphere. This exercise included sensitivity testing using alternate latitude combinations to account for displacement of eddy circulations off the equator as was reported by Randel (1992), Dickinson and Molinari (2002), and Kerns and Chen (2014). The outcome of this objective census of equatorial wave activity will be reported in a separate study, but of relevance here, the results reveal that the westward MRG-like and eastward EIG-like circulations detected in Fig. 11 are present from the surface to around 700 hPa. Above this level the signals weaken rapidly near the date line and strengthen somewhat over the Indian sector but in the lower-frequency range as in the westward signals of Figs. 11c and 11d. As mentioned above, these eddies display some coupling to convection but this coherence is much lower than in Fig. 11a over the central Pacific. Between 150 and 100 hPa, signals with periods centered on 3 days begin to appear over the Indian sector, and these spread to all longitudes and strengthen rapidly into the stratosphere, with the strongest evidence for stratospheric MRG–EIG circulations at 50 hPa as in Figs. 9b and 9c.

In summary, synoptic-scale eddies centered on the equator are detectable at most longitudes within the troposphere, but these are most strongly coupled to convection in the 3–5-day range for lower-tropospheric circulations over the central and eastern Pacific, Atlantic, and Africa. There is also some evidence of weaker convective coupling between mid- and upper-tropospheric MRG-like eddies over the Indian sector but at a lower-frequency corresponding to periods in the 5–10-day range. Thus, the cross-spectral results described here confirm that the global $n = 0$ T_b spectral signal in the 2–6-day range in Fig. 1a is dominated by the activity over the central Pacific, as was also inferred by the original studies of Liebmann and Hendon (1990) and Hendon and Liebmann (1991), as well as by Dias and Kiladis (2014).

6. Seasonality and temporal variability

Substantial variability in MRG–EIG activity is seen across a wide range of time scales (Dunkerton and Baldwin 1995). As with indices of the MJO such as RMM (Wheeler and Hendon 2004) and OMI (Kiladis et al. 2014), metrics of MRG–EIG activity can be obtained from their PC time series. To extend the temporal coverage of this wave activity we have recalculated EOFs discussed above using twice-daily OLR data from 1974 to 2014, with nearly indistinguishable results for the period of overlap between the two datasets apart from a rescaling that arises from the difference between T_b and OLR.

It is well known that MRG activity is maximized during the boreal summer and fall (Liebmann and Hendon 1990; Hendon and Liebmann 1991; Dunkerton

1993; Dunkerton and Baldwin 1995; Magaña and Yanai 1995; Roundy and Frank 2004; Huang and Huang 2011; Horinouchi 2013) along with convective signals associated with the EIG portion of the spectrum (Wheeler and Kiladis 1999; Dias and Kiladis 2014). Figure 12 shows the monthly mean standard deviation (std dev) of the PCs associated with the four EOFs of T_{b26} and T_{b26}^{w} discussed in Figs. 5 and 8. For both the standing and westward-propagating cases, there is activity throughout the year, with a minimum during northern winter and peaks in late summer and fall.

A time series of the monthly average std dev of the PCs associated with the first two EOFs of T_{b26} from Fig. 5 during 1990–99 is shown in Fig. 13. Apart from the obvious seasonal cycle, there is also large intraseasonal to interannual MRG–EIG variability. One feature seen in Fig. 13 is the suppressed activity during 1997—a period of strong El Niño conditions. A similar suppression is also detectable during other years of anomalously warm equatorial Pacific sea surface temperature (SST) such as the early 1990s, and during 1982 and 1987, as well as for the westward-propagating modes in Fig. 8 (not shown), consistent with previous studies (e.g., Chang and Miller 1977; Yanai and Lu 1983; Dunkerton 1993; Takayabu and Nitta 1993; Yang and Hoskins 2013). In their study of interannual variability of CCEWs, Huang and Huang (2011) also found a negative correlation between equatorial SST and convective activity associated with MRGs and most other CCEWs at the latitude of the ITCZ, along with increased convective activity along the equator.

To further investigate the nature of this interannual variability, we calculate an anomalous monthly std dev for each PC by subtracting its respective climatological monthly mean std dev for the period 1979–2014. The monthly activity of the two PCs depicted in Fig. 13 deseasonalized in this way is correlated at 0.40, which is much higher than the 0.19 correlation between the corresponding four-times-daily raw PCs obtained in section 4. We similarly calculate monthly anomalies as above of the Niño-3.4, Niño-3, and Niño-4 indices commonly used to measure the state of the El Niño–Southern Oscillation (ENSO). The correlation is negative and statistically significant, though weak, between all of the PC std dev series and the Niño-3 and Niño-3.4 indices, peaking at −0.32 and −0.30 between Niño-3 and for activity of the pair of PCs that represent the westward 2–6-day MRG patterns in Fig. 8. Interestingly, the Niño-3 region represents SST fluctuations from 5°S to 5°N and from 150° to 90°W and is the index based on SST farthest away from the center of MRG–EIG convective activity represented by the EOFs, whereas the correlations with the Niño-4 index that is more centered near the date line

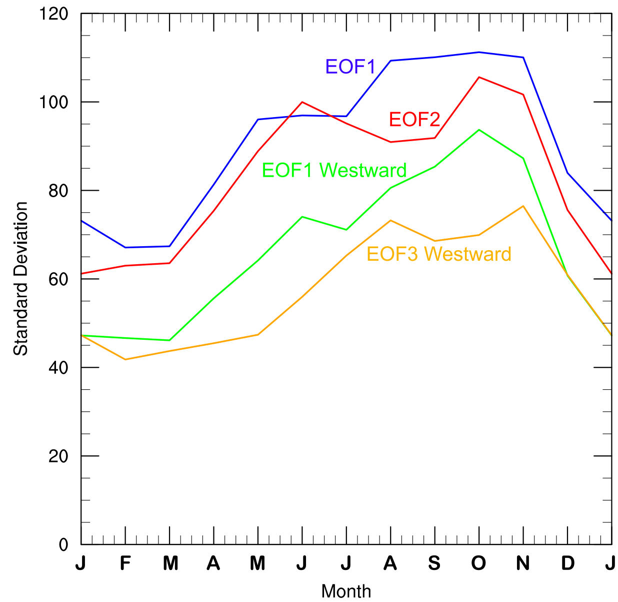

FIG. 12. Monthly mean standard deviation of the 2–6-day-filtered (blue, red) and 2–6-day westward-filtered (green, yellow) OLR PCs corresponding to the T_{b26} EOFs in Fig. 5 and T_{b26}^{w} EOFs in Fig. 8, respectively, averaged over the period 1979–2014.

are effectively zero. This indicates that the activity is affected more by large-scale changes in the basic state as opposed to being driven more by local SST.

Horinouchi (2013) also found a weak but negative correlation between MRG activity and equatorial SST using a somewhat different measure based on MRG filtered OLR as well as a strong positive (negative) correlation with anomalous seasonal equatorial precipitation (OLR). We examine this aspect by correlating the monthly OLR anomalies at each grid point with each monthly PC std dev anomaly time series as was done above for the ENSO indices. In every case, monthly MRG–EIG activity was positively correlated with monthly OLR anomalies along the equator and negatively correlated within the mean position of the ITCZ throughout the entire equatorial Pacific. While this supports the hypothesis of Horinouchi (2013) that increased MRG activity should be associated with a decrease in convective activity along the equator, the correlations were small, peaking at only around 0.40 near the date line for the westward-propagating MRG mode in Fig. 8a (not shown). It turns out that this signal is also primarily driven by ENSO, which becomes evident when looking at lagged relationships, since the correlations are very persistent and evolve slowly over monthly time scales. Taken together, the results of this section do provide some evidence for the idea that MRG–EIG activity is favored where there is a minimum in equatorial SST and a strong double ITCZ (Hendon and Liebmann 1991) and that this favorable configuration is disrupted by El Niño. Investigation of the origin of other

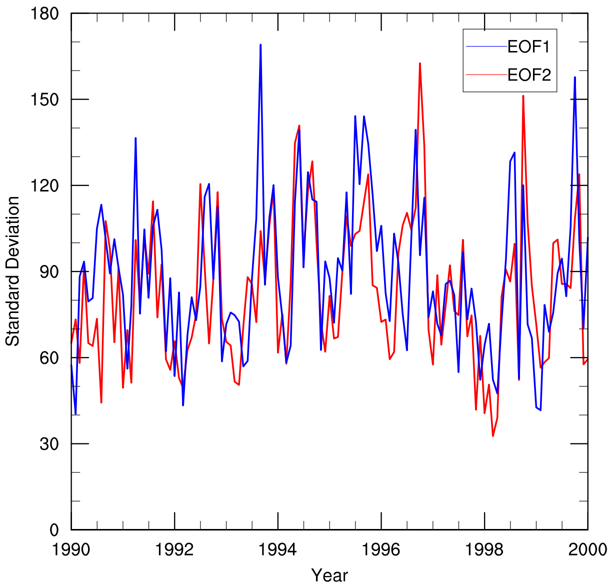

FIG. 13. Monthly mean standard deviation of the OLR PCs corresponding to the T_{b26} EOFs in Fig. 5, for individual months during the period 1990–99 (see text).

large variations in activity such as those illustrated in Fig. 13 is ongoing and will be reported in a future study.

7. Upper-tropospheric structure

While the evolution of T_b and lower-tropospheric circulations associated with each of the MRG–EIG modes differ little throughout the year, this is not the case in the upper troposphere. As an example, Fig. 14 shows the evolution of 200-hPa flow associated with EOF1 at half-day intervals from day −1 through day 0, obtained by calculating June–August-only EOFs of T_{b26} for the same Pacific domain as before. In general, these results, or those for any season, are very similar to those derived by using the annual EOFs described in section 4, and since the lower-tropospheric patterns are also very similar (not shown), this pattern can be compared directly with the annual pattern at 850 hPa in Fig. 6. Southward cross-equatorial flow opposing that at 850 hPa is seen near the date line in Fig. 14c, although this is not associated with an equatorial gyre but rather an anticyclonic perturbation on the northwest side of the enhanced ITCZ convective signal. Tracing the evolution back in time, Fig. 14 shows that this feature separated off from a cyclone initially at 20°S, 140°W that extended to the equator in Fig. 14a. A strikingly similar evolution of upper-level MRG features was noted by Magaña and Yanai (1995), including a strong association with the southern storm track, although the basis for their analysis used correlations against 3–12-day-filtered 200-hPa

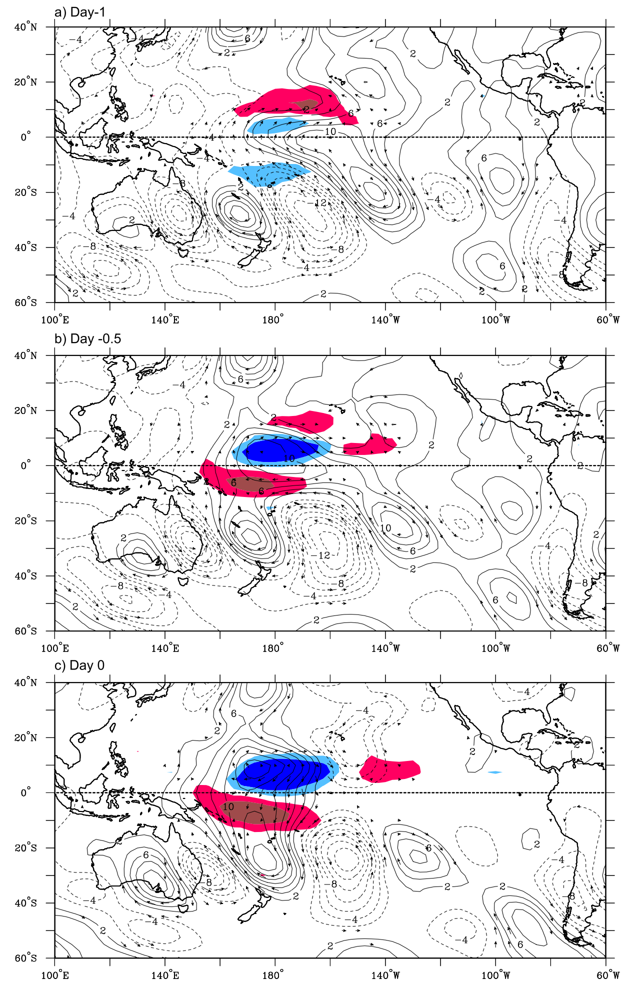

FIG. 14. As in Fig. 5, but for T_{b26} EOF1 at 200 hPa calculated using only June–August data at (a) day −1, (b) day −0.5, and (c) day 0. Streamfunction contour interval is $2 \times 10^5\ \mathrm{m^2\,s^{-1}}$. The largest wind vectors correspond to speeds of around $4\ \mathrm{m\,s^{-1}}$.

equatorial meridional wind at the date line rather than the T_{b26} EOF used here.

The eddy pattern along 30°S in Fig. 14 represents the eastern portion of a wave train propagating into lower latitudes from the southern Indian Ocean. Figure 15 shows a global view of the 200-hPa streamfunction at day−9, where a statistically significant, continuous wave train is seen originating over the South Atlantic, which then arcs into the subtropical jet over and to the east of Australia. Such a signal was not only seen by Magaña and Yanai (1995) associated with MRG activity (their Fig. 10a), but a very similar pattern was also obtained by Straub and Kiladis (2003a) prior to the development of convectively coupled Kelvin waves in the ITCZ (their Fig. 2). Similar precursor wave trains are also obtained for the second EOF in Fig. 5b, despite its higher-wavenumber structure, and

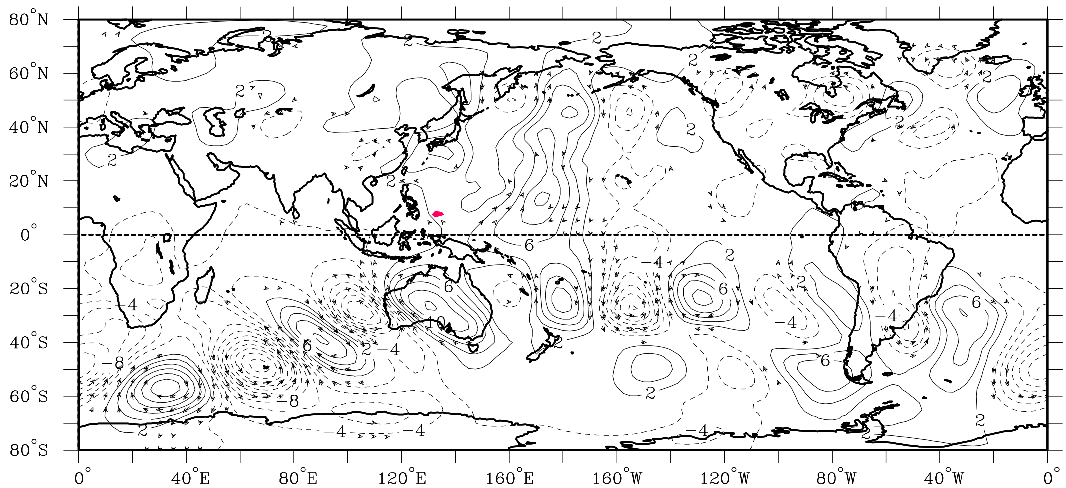

FIG. 15. As in Fig. 14, but for day−9.

the westward-propagating MRG mode in Fig. 8a, but not for the pattern in Fig. 8b. Notwithstanding some differences in the phasing of these waves, it thus appears that at least Kelvin, MRG, and the zonally standing modes studied here can be similarly forced by incoming wave activity originating in the southern extratropics during austral winter.

As a contrasting example, Fig. 16 shows the evolution of 200-hPa flow for EOF1 calculated from December–February T_{b26} data only. Although the evolution of T_b and lower-tropospheric flow are again very similar to the annual pattern in Fig. 6 and that for June–August (not shown), the upper troposphere is now dominated by wave activity originating in the North Pacific storm track. As this wave train tracks eastward and equatorward into the eastern Pacific, a clockwise eddy separates from an extratropical anticyclonic flow and moves westward along the equator to the west side of active ITCZ convection at day 0 (Figs. 16b,c). As in June–August (Fig. 15), a statistically significant extratropical wave train exists for several days before the onset of equatorial convection, but in this case it emanates from Asia (not shown).

The sequence of Fig. 16 is typical of the equatorward propagation resulting from Rossby wave propagation into the "westerly duct" region during northern winter (Webster and Holton 1982; Kiladis and Weickmann 1992a,b, 1997; Tomas and Webster 1994). Along with studies cited above, such wave activity has been implicated in exciting a variety of equatorial modes including MRGs, equatorial Rossby waves, and Kelvin waves in observations (Kiladis and Wheeler 1995; Kiladis 1998; Yang et al. 2007b; Yang and Hoskins 2013) and in simple models (e.g., Lim and Chang 1981; Itoh and Ghil 1988; Zhang and Webster 1992; Zhang 1993; Hoskins and Yang 2000; Biello and Majda 2004; Ferguson et al. 2009). The idea that lateral forcing is important for equatorial wave initiation is also in accord with observational results of Zangvil and Yanai (1980), Yanai and Lu (1983), and Randel (1992), who found significant meridional convergence of wave activity fluxes associated with upper-tropospheric MRG activity. Note that our approach does not explicitly measure wave activity associations per se but, rather, is dependent on the specific timing and phasing of individual synoptic-scale events between the tropics and higher latitudes. It is evident that the upper-tropospheric equatorial eddies depicted in Figs. 14 and 16 are not very reminiscent of MRG modes—consistent with the spectral results discussed in section 6. Also notable is the fact that during the transition seasons, even though very similar T_b EOFs are obtained, there is little evidence of extratropical forcing (not shown). This is consistent with the notion that the extratropical wave activity identified here is only one possible mechanism for the excitation of the equatorial modes, which likely also includes local forcing by convection (e.g., Hayashi 1970; Itoh and Ghil 1988; Khouider et al. 2013) or interference with other equatorial modes (e.g., Raupp and Silva Dias 2005).

8. Summary and discussion

The connection between the westward and eastward spectral peaks of antisymmetric space–time T_b (Fig. 1a) has motivated us to address the question of whether this signal represents a continuum of wave activity or whether convectively coupled $n = 0$ MRGs and EIGs occur independently of each other. Using EOF analysis of T_b filtered at 2–6 days T_{b26}, which brackets the

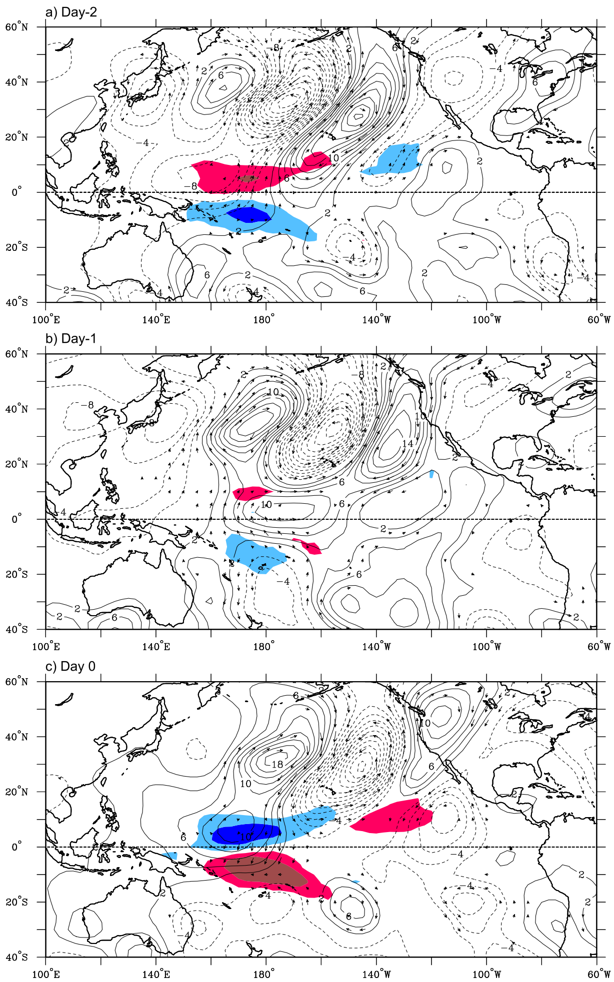

FIG. 16. As in Fig. 14, but for T_{b26} EOF1 at 200 hPa calculated using only December–February data at (a) day −2, (b) day −1, and (c) day 0.

frequencies of the MRG–EIG signals, we isolated a zonally stationary convective mode that is antisymmetric about the equator and primarily confined to the west-central Pacific equatorial region near the date line. This mode appears to correspond to the standing cloudiness signals originally documented by Wallace (1971) and also noted by Takayabu and Nitta (1993). A new finding is that the T_{b26} signal and associated deep convection are not completely stationary but, instead, propagate meridionally with signals of one sign forming near the equator that move poleward to beyond the mean latitudes of the ITCZ and SPCZ, to be replaced by opposite-signed convective signals that in turn also propagate meridionally (Fig. 6). Associated with this evolution are MRG-like circulations that propagate westward through the convective signals, with no evidence of eastward-propagating EIG circulations in the EOF analysis.

Nevertheless, strong evidence of EIG circulations is seen in cross spectra. Our hypothesis, discussed in further detail in Part II, is that the statistical signal isolated here results from a mixture of westward and eastward propagating, along with zonally standing events that represent predominantly MRG or EIG modes that at times constructively interfere to produce a standing T_{b26} signal. We also propose that MRG circulations dominate the synoptic time scales despite the prevalence of zonally standing cloudiness signals because EIGs have much weaker rotational winds than MRGs for a given amount of divergence. This last point would account for the fact that MRGs have been studied almost to the exclusion of EIGs in the literature, even though the signal of EIGs is if anything even more prominent than MRGs in space–time spectra of T_b (Fig. 1a). Although the EIG portion of the spectrum is not as prominent in the case of dynamical fields at 50 hPa (e.g., Fig. 1b), cross-spectral evidence like that in Fig. 9 also supports the existence of EIG activity within the lower stratosphere (not shown). The nature of the MRG–EIG continuum in the stratosphere will be further investigated in a separate study.

It is well known that the ITCZ and SPCZ vary coherently over a wide range of space and time scales. On interannual time scales, they tend to vary in phase, with a tendency for both to be enhanced and to shift equatorward during El Niño conditions (e.g., Chung and Power 2015), with opposite tendencies during La Niña. This in phase variability is also observed on intraseasonal time scales associated with the MJO (e.g., Matthews and Kiladis 1999). However, at synoptic time scales we have shown that out-of-phase variability is more dominant owing to the antisymmetric nature of the divergence associated with the $n = 0$ Matsuno modes. The localization of the MRG–EIG convective signal to the west-central Pacific is another intriguing issue. This extent of this localization is not necessarily reflected in maps of MRG–EIG T_b variance that have been published in past literature (e.g., Wheeler and Kiladis 1999; Roundy and Frank 2004; Kiladis et al. 2009; Huang and Huang 2011), which we strongly suspect are unduly influenced by unrelated background variance in regions outside the west-central Pacific. It would be of great interest to evaluate general circulation models with respect to their abilities to simulate this localization and to assess the extent to which this is related to the presence of realistic versus erroneous ''double ITCZs'' in the basic states of such simulations.

Several other unresolved questions remain regarding the dynamics of MRGs–EIGs. The poleward and eastward meridional tilts of the convective signals are especially pronounced for the T^{w}_{b26} EOFs in Fig. 8a, with less-exaggerated tilts in the circulation fields. This results in substantial deviations from the symmetric structures of Matsuno's linear shallow-water theory on an equatorial beta plane. Such anisotropies are common features in theoretical and simple numerical models that include wave–conditional instability of the second kind-type convective coupling mechanisms (Hayashi 1970) or horizontal or vertical shear (e.g., Kasahara and Silva Dias 1986; Wang and Xie 1996; Han and Khouider 2010). A separate mechanism has been attributed to the nontraditional Coriolis terms (Roundy and Janiga 2012) associated with the horizontal component of Earth angular velocity (Kasahara 2003). It turns out that parameters such as meridional wind and temperature associated with zonally standing T_{b26} have little zonal tilt in the vertical, although they do propagate upward in the troposphere up to about 200 hPa and downward above that level and into the stratosphere in lagged vertical cross sections (not shown). This is in line with the theoretical response to a midtropospheric antisymmetric zonally standing but timevarying heat source [see Fig. 10 of Holton (1972)], although further analysis is required to determine whether this signal results from interference between alternating MRG and EIG signals.

While there is strong evidence for extratropical forcing of MRG–EIG activity in this and many previous studies, the precise dynamics responsible for this presumed forcing have yet to be fully uncovered. In addition, the mechanisms responsible for the meridional propagation in T_{b26} are currently being studied in detail. As mentioned above, this signal is also present in TRMM 3B42 precipitation data and, so, is likely not simply due to the advection of upper-level cloudiness. An analysis of moisture flux indicates that low-level moisture convergence also propagates poleward and leads the precipitation and cloudiness signals of the meridionally propagating T_{b26} signals in Fig. 6 (not shown). A moisture budget analysis, using the same NCEP reanalysis data as in a recent study by Newman et al. (2012), is currently underway and this will also be extended using high-resolution ERAI data. Preliminary results indicate that the interplay between the zonal and meridional components of the divergent flow with the basic state moisture field is responsible for the meridional propagation of the T_{b26} EOF. As is shown in Part II, a distinct difference in the zonal and meridional components of the divergent wind between MRGs and EIGs is present in both Matsuno's theory and in observations and is likely tied into the root cause for the zonally standing component of the T_{b26} signal.

Acknowledgments. We thank Brant Liebmann, Takeshi Horinouchi, and two anonymous reviewers for their insightful comments on an initial draft of this manuscript. ERA-Interim data was provided by NCAR.

REFERENCES

Aiyyer, A. R., and J. Molinari, 2003: Evolution of mixed Rossby–gravity waves in idealized MJO environments. *J. Atmos. Sci.*, **60**, 2837–2855, doi:10.1175/1520-0469(2003)060<2837:EOMRWI>2.0.CO;2.

Alexander, M. J., and D. A. Ortland, 2010: Equatorial waves in High Resolution Dynamics Limb Sounder (HIRDLS) data. *J. Geophys. Res.*, **115**, D24111, doi:10.1029/2010JD014782.

Alexander, S. P., T. Tsuda, and Y. Kawatani, 2008a: COSMIC GPS observations of Northern Hemisphere winter stratospheric gravity waves and comparisons with an atmospheric general circulation model. *Geophys. Res. Lett.*, **35**, L10808, doi:10.1029/2008GL033174.

——, ——, ——, and M. Takahashi, 2008b: Global distribution of atmospheric waves in the equatorial upper troposphere and lower stratosphere: COSMIC observations of wave mean flow interactions. *J. Geophys. Res.*, **113**, D24115, doi:10.1029/2008JD010039.

Baldwin, M. P., and Coauthors, 2001: The quasi-biennial oscillation. *Rev. Geophys.*, **39**, 179–229, doi:10.1029/1999RG000073.

Bergman, J. W., and M. L. Salby, 1994: Equatorial wave activity derived from fluctuations in observed convection. *J. Atmos. Sci.*, **51**, 3791–3806, doi:10.1175/1520-0469(1994)051<3791:EWADFF>2.0.CO;2.

Biello, J., and A. J. Majda, 2004: Boundary layer dissipation and the nonlinear interaction of equatorial baroclinic and barotropic Rossby waves. *Geophys. Astrophys. Fluid Dyn.*, **98**, 85–127, doi:10.1080/03091920410001686712.

Blackman, R. B., and J. Tukey, 1958: *The Measurement of Power Spectra.* Dover, 190 pp.

Blandford, R., 1965: Mixed gravity-Rossby waves in the ocean. *Deep-Sea Res. Oceanogr. Abstr.*, **13**, 941–961, doi:10.1016/0011-7471(76)90912-8.

Chang, C.-P., 1970: Westward propagating cloud patterns in the tropical Pacific as seen from composite satellite photographs. *J. Atmos. Sci.*, **27**, 133–138, doi:10.1175/1520-0469(1970)027<0133:WPCPIT>2.0.CO;2.

——, 1973: A dynamical model of the Intertropical Convergence Zone. *J. Atmos. Sci.*, **30**, 190–212, doi:10.1175/1520-0469(1973)030<0190:ADMOTI>2.0.CO;2.

——, and C. R. Miller, 1977: Comparison of easterly waves in the tropical Pacific during two contrasting periods of sea surface temperature anomalies. *J. Atmos. Sci.*, **34**, 615–628, doi:10.1175/1520-0469(1977)034<0615:COEWIT>2.0.CO;2.

Chen, G., and R. Huang, 2009: Interannual variations in mixed Rossby–gravity waves and their impacts on tropical cyclogenesis over the western North Pacific. *J. Climate*, **22**, 535–549, doi:10.1175/2008JCLI2221.1.

Chen, S., and Coauthors, 2015: A study of CINDY/DYNAMO MJO suppressed phase. *J. Atmos. Sci.*, **72**, 3755–3779, doi:10.1175/JAS-D-13-0348.1.

Chung, C. T. Y., and S. B. Power, 2015: Modelled rainfall response to strong El Niño sea surface temperature anomalies in the tropical Pacific. *J. Climate*, **28**, 3133–3151, doi:10.1175/JCLI-D-14-00610.1.

Dias, J., and G. N. Kiladis, 2014: Influence of the basic state zonal flow on convectively coupled equatorial waves. *Geophys. Res. Lett.*, **41**, 6904–6913, doi:10.1002/2014GL061476.

——, and ——, 2016: The relationship between equatorial mixed Rossby–gravity and eastward inertio-gravity waves. Part II. *J. Atmos. Sci.*, **73**, 2147–2163, doi:10.1175/JAS-D-15-0231.1.

Dickinson, M., and J. Molinari, 2002: Mixed Rossby–gravity waves and western Pacific tropical cyclogenesis. Part I: Synoptic evolution. *J. Atmos. Sci.*, **59**, 2183–2196, doi:10.1175/1520-0469(2002)059<2183:MRGWAW>2.0.CO;2.

Dunkerton, T. J., 1991: Intensity variation and coherence of 3–6 day equatorial waves. *Geophys. Res. Lett.*, **18**, 1469–1472, doi:10.1029/91GL01780.

——, 1993: Observation of 3–6-day meridional wind oscillations over the tropical Pacific, 1973–1992: Vertical structure and interannual variability. *J. Atmos. Sci.*, **50**, 3292–3307, doi:10.1175/1520-0469(1993)050<3292:OODMWO>2.0.CO;2.

——, 1997: The role of gravity waves in the quasi-biennial oscillation. *J. Geophys. Res.*, **102**, 26 053–26 076, doi:10.1029/96JD02999.

——, and M. P. Baldwin, 1995: Observation of 3–6-day meridional wind oscillations over the tropical Pacific, 1973–1992: Horizontal structure and propagation. *J. Atmos. Sci.*, **52**, 1585–1601, doi:10.1175/1520-0469(1995)052<1585:OODMWO>2.0.CO;2.

Ern, M., P. Preusse, M. Krebsbach, M. G. Mlynczak, and J. M. Russell III, 2008: Equatorial wave analysis from SABER and ECMWF temperatures. *Atmos. Chem. Phys.*, **8**, 845–869, doi:10.5194/acp-8-845-2008.

Ferguson, J., B. Khouider, and M. Namazi, 2009: Two-way interactions between equatorially-trapped waves and the barotropic flow. *Chin. Ann. Math.*, **30B**, 539–568, doi:10.1007/s11401-009-0102-9.

Frank, W. M., and P. E. Roundy, 2006: The role of tropical waves in tropical cyclogenesis. *Mon. Wea. Rev.*, **134**, 2397–2417, doi:10.1175/MWR3204.1.

Fritts, D. C., and M. J. Alexander, 2003: Gravity wave dynamics and effects in the middle atmosphere. *Rev. Geophys.*, **41**, 1003, doi:10.1029/2001RG000106.

Gehne, M., and R. Kleeman, 2012: Spectral analysis of tropical atmospheric dynamical variables using a linear shallow-water modal decomposition. *J. Atmos. Sci.*, **69**, 2300–2316, doi:10.1175/JAS-D-10-05008.1.

Han, Y., and B. Khouider, 2010: Convectively coupled waves in a sheared environment. *J. Atmos. Sci.*, **67**, 2913–2942, doi:10.1175/2010JAS3335.1.

Hayashi, Y., 1970: A theory of large-scale equatorial waves generated by condensation heat and accelerating the zonal wind. *J. Meteor. Soc. Japan.*, **48**, 140–160.

Hendon, H. H., and B. Liebmann, 1991: The structure and annual variation of antisymmetric fluctuations of tropical convection and their association with Rossby–gravity waves. *J. Atmos. Sci.*, **48**, 2127–2140, doi:10.1175/1520-0469(1991)048<2127:TSAAVO>2.0.CO;2.

——, and M. C. Wheeler, 2008: Some space–time spectral analyses of tropical convection and planetary-scale waves. *J. Atmos. Sci.*, **65**, 2936–2948, doi:10.1175/2008JAS2675.1.

Hodges, K. I., D. W. Chappell, and G. J. Robinson, 2000: An improved algorithm for generating global window brightness temperatures from multiple satellite infrared imagery. *J. Atmos. Oceanic Technol.*, **17**, 1296–1312, doi:10.1175/1520-0426(2000)017<1296:AIAFGG>2.0.CO;2.

Holton, J. R., 1972: Waves in the equatorial stratosphere generated by tropospheric heat sources. *J. Atmos. Sci.*, **29**, 368–375, doi:10.1175/1520-0469(1972)029<0368:WITESG>2.0.CO;2.

——, J. M. Wallace, and J. A. Young, 1971: On boundary layer dynamics and the ITCZ. *J. Atmos. Sci.*, **28**, 275–280, doi:10.1175/1520-0469(1971)028<0275:OBLDAT>2.0.CO;2.

Horinouchi, T., 2013: Modulation of seasonal precipitation over the tropical western/central Pacific by convectively coupled mixed Rossby–gravity waves. *J. Atmos. Sci.*, **70**, 600–606, doi:10.1175/JAS-D-12-0283.1.

Hoskins, B. J., and G.-Y. Yang, 2000: The equatorial response to higher-latitude forcing. *J. Atmos. Sci.*, **57**, 1197–1213, doi:10.1175/1520-0469(2000)057<1197:TERTHL>2.0.CO;2.

Huang, P., and R. Huang, 2011: Climatology and interannual variability of convectively coupled equatorial waves activity. *J. Climate*, **24**, 4451–4465, doi:10.1175/2011JCLI4021.1.

Huffman, G. J., and Coauthors, 2007: The TRMM Multisatellite Precipitation Analysis (TMPA): Quasi-global, multiyear, combined-sensor precipitation estimates at fine scales. *J. Hydrometeor.*, **8**, 38–55, doi:10.1175/JHM560.1.

Itoh, H., and M. Ghil, 1988: The generation mechanism of mixed Rossby-gravity waves in the equatorial troposphere. *J. Atmos. Sci.*, **45**, 585–604, doi:10.1175/1520-0469(1988)045<0585:TGMOMR>2.0.CO;2.

Kasahara, A., 2003: On the nonhydrostatic atmospheric models with inclusion of the horizontal component of the Earth's angular velocity. *J. Meteor. Soc. Japan*, **81**, 935–950, doi:10.2151/jmsj.81.935.

——, and P. L. Silva Dias, 1986: Response of planetary waves to stationary tropical heating in a global atmosphere with meridional and vertical shear. *J. Atmos. Sci.*, **43**, 1893–1912, doi:10.1175/1520-0469(1986)043<1893:ROPWTS>2.0.CO;2.

Kawatani, Y., S. Watanabe, K. Sato, T. J. Dunkerton, S. Miyahara, and M. Takahashi, 2010: The roles of equatorial trapped waves and internal inertia–gravity waves in driving the quasi-biennial oscillation. Part I: Zonal mean wave forcing. *J. Atmos. Sci.*, **67**, 963–980, doi:10.1175/2009JAS3222.1.

Kerns, B. W., and S. S. Chen, 2014: Equatorial dry air intrusion and related synoptic variability in MJO initiation during DYNAMO. *Mon. Wea. Rev.*, **142**, 1326–1343, doi:10.1175/MWR-D-13-00159.1.

Khouider, B., A. J. Majda, and S. N. Stechmann, 2013: Climate science in the tropics: Waves, vortices and PDEs. *Nonlinearity*, **26**, R1–R68, doi:10.1088/0951-7715/26/1/R1.

Kiladis, G. N., 1998: Observations of Rossby waves linked to convection over the eastern tropical Pacific. *J. Atmos. Sci.*, **55**, 321–339, doi:10.1175/1520-0469(1998)055<0321:OORWLT>2.0.CO;2.

——, and K. M. Weickmann, 1992a: Circulation anomalies associated with tropical convection during northern winter. *Mon. Wea. Rev.*, **120**, 1900–1923, doi:10.1175/1520-0493(1992)120<1900:CAAWTC>2.0.CO;2.

——, and ——, 1992b: Extratropical forcing of tropical Pacific convection during northern winter. *Mon. Wea. Rev.*, **120**, 1924–1939, doi:10.1175/1520-0493(1992)120<1924:EFOTPC>2.0.CO;2.

——, and M. Wheeler, 1995: Horizontal and vertical structure of observed tropospheric equatorial Rossby waves. *J. Geophys. Res.*, **100**, 22 981–22 997, doi:10.1029/95JD02415.

——, and K. M. Weickmann, 1997: Horizontal structure and seasonality of large-scale circulations associated with submonthly tropical convection. *Mon. Wea. Rev.*, **125**, 1997–2013, doi:10.1175/1520-0493(1997)125<1997:HSASOL>2.0.CO;2.

——, M. C. Wheeler, P. T. Haertel, K. H. Straub, and P. E. Roundy, 2009: Convectively coupled equatorial waves. *Rev. Geophys.*, **47**, RG2003, doi:10.1029/2008RG000266.

——, J. Dias, K. H. Straub, M. C. Wheeler, S. N. Tulich, K. Kikuchi, K. M. Weickmann, and M. J. Ventrice, 2014: A comparison of OLR and circulation-based indices for tracking the MJO. *Mon. Wea. Rev.*, **142**, 1697–1715, doi:10.1175/MWR-D-13-00301.1.

Kuo, H.-C., J.-H. Chen, R. T. Williams, and C.-P. Chang, 2001: Rossby waves in zonally opposing mean flow: Behavior in Northwest

Pacific summer monsoon. *J. Atmos. Sci.*, **58**, 1035–1050, doi:10.1175/1520-0469(2001)058<1035:RWIZOM>2.0.CO;2.

Liebmann, B., and H. H. Hendon, 1990: Synoptic-scale disturbances near the equator. *J. Atmos. Sci.*, **47**, 1463–1479, doi:10.1175/1520-0469(1990)047<1463:SSDNTE>2.0.CO;2.

——, and C. A. Smith, 1996: Description of a complete (interpolated) outgoing longwave radiation dataset. *Bull. Amer. Meteor. Soc.*, **77**, 1275–1277.

Lim, H., and C. P. Chang, 1981: A theory for midlatitude forcing of tropical motions during winter monsoons. *J. Atmos. Sci.*, **38**, 2377–2392, doi:10.1175/1520-0469(1981)038<2377:ATFMFO>2.0.CO;2.

Lindzen, R. S., and J. R. Holton, 1968: A theory of the quasi-biennial oscillation. *J. Atmos. Sci.*, **25**, 1095–1107, doi:10.1175/1520-0469(1968)025<1095:ATOTQB>2.0.CO;2.

Livezey, R. E., and W. Y. Chen, 1983: Statistical field significance and its determination by Monte Carlo techniques. *Mon. Wea. Rev.*, **111**, 46–59, doi:10.1175/1520-0493(1983)111<0046:SFSAID>2.0.CO;2.

Lott, F., J. Kuttippurath, and F. Vial, 2009: A climatology of the gravest waves in the equatorial lower and middle stratosphere: Method and results for the ERA-40 Re-Analysis and the LMDz GCM. *J. Atmos. Sci.*, **66**, 1327–1346, doi:10.1175/2008JAS2880.1.

Madden, R. A., 2007: Large-scale, free Rossby waves in the atmosphere—An update. *Tellus*, **59A**, doi:10.3402/tellusa.v59i5.15155.

——, and P. R. Julian, 1972: Description of global-scale circulation cells in the tropics with a 40–50 day period. *J. Atmos. Sci.*, **29**, 1109–1123, doi:10.1175/1520-0469(1972)029<1109:DOGSCC>2.0.CO;2.

Magaña, V., and M. Yanai, 1995: Mixed Rossby–gravity waves triggered by lateral forcing. *J. Atmos. Sci.*, **52**, 1473–1486, doi:10.1175/1520-0469(1995)052<1473:MRWTBL>2.0.CO;2.

Maruyama, T., 1967: Large-scale disturbances in the equatorial lower stratosphere. *J. Meteor. Soc. Japan*, **45**, 391–408.

——, 1968: Upward transport of westerly momentum due to large-scale disturbances in the lower stratosphere. *J. Meteor. Soc. Japan*, **46**, 404–417.

——, 1991: Annual and QBO-synchronized variations of lower-stratospheric equatorial wave activity over Singapore during 1961-1989. *J. Meteor. Soc. Japan*, **69**, 219–232.

——, and M. Yanai, 1967: Evidence of large scale wave disturbances in the equatorial lower stratosphere. *J. Meteor. Soc. Japan*, **45**, 196–199.

Matsuno, T., 1966: Quasi-geostrophic motions in the equatorial area. *J. Meteor. Soc. Japan*, **44**, 25–43.

Matthews, A. J., and G. N. Kiladis, 1999: The tropical–extratropical interaction between high-frequency transients and the Madden–Julian Oscillation. *Mon. Wea. Rev.*, **127**, 661–677, doi:10.1175/1520-0493(1999)127<0661:TTEIBH>2.0.CO;2.

Maury, P., and F. Lott, 2014: On the presence of equatorial waves in the lower stratosphere of a general circulation model. *Atmos. Chem. Phys.*, **14**, 1869–1880, doi:10.5194/acp-14-1869-2014.

Mayr, H. G., J. G. Mengel, E. R. Talaat, H. S. Porter, and K. L. Chan, 2003: Planetary-scale inertio gravity waves in the mesosphere. *Geophys. Res. Lett.*, **30**, 2228, doi:10.1029/2003GL018376.

——, ——, ——, ——, and ——, 2004: Properties of internal planetary-scale inertio gravity waves in the mesosphere. *Ann. Geophys.*, **22**, 3421–3435, doi:10.5194/angeo-22-3421-2004.

Molinari, J. D., K. Lombardo, and D. Vollaro, 2007: Tropical cyclogenesis within an equatorial Rossby wave packet. *J. Atmos. Sci.*, **64**, 1301–1317, doi:10.1175/JAS3902.1.

Monahan, A. H., J. C. Fyfe, M. H. P. Ambaum, D. B. Stephenson, and G. R. North, 2009: Empirical orthogonal functions: The medium is the message. *J. Climate*, **22**, 6501–6514, doi:10.1175/2009JCLI3062.1.

Muraleedharan, P. M., S. Prasanna Kumar, K. Mohana Kumar, S. Sijikumar, K. U. Sivakumar, and T. Mathew, 2015: Observational evidence of mixed Rossby gravity waves at the central equatorial Indian Ocean. *Meteor. Atmos. Phys.*, **127**, 407–417, doi:10.1007/s00703-015-0376-2.

Newman, M., G. N. Kiladis, K. M. Weickmann, F. M. Ralph, and P. D. Sardeshmukh, 2012: Relative contributions of synoptic and low-frequency eddies to time-mean atmospheric moisture transport, including the role of atmospheric rivers. *J. Climate*, **25**, 7341–7361, doi:10.1175/JCLI-D-11-00665.1.

Nitta, T., 1970: Statistical study of tropospheric wave disturbances in the tropical Pacific region. *J. Meteor. Soc. Japan*, **48**, 47–60.

North, G. R., T. L. Bell, R. F. Cahalan, and F. J. Moeng, 1982: Sampling errors in the estimation of empirical orthogonal functions. *Mon. Wea. Rev.*, **110**, 699–706, doi:10.1175/1520-0493(1982)110<0699:SEITEO>2.0.CO;2.

Numaguti, A., 1995: Characteristics of 4-to-20-day-period disturbances observed in the equatorial Pacific during the TOGA COARE IOP. *J. Meteor. Soc. Japan*, **73**, 353–377.

Randel, W. J., 1992: Upper tropospheric equatorial waves in ECMWF analyses. *Quart. J. Roy. Meteor. Soc.*, **118**, 365–394, doi:10.1002/qj.49711850409.

Rattray, M. J., 1965: Time-dependent motion in an ocean, a unified two-layer, beta-plane approximation. *Studies on Oceanography, Hidaka Memorial Volume*, K. Yoshida, Ed., Department of Oceanography, University of Washington, 19–29.

——, and R. L. Charnell, 1966: Quasigeostrophic free oscillations in enclosed basins. *J. Mar. Res.*, **24**, 82–103.

Raupp, C. F. M., and P. L. Silva Dias, 2005: Excitation mechanism of mixed Rossby–gravity waves in the equatorial atmosphere: Role of the nonlinear interactions among equatorial waves. *J. Atmos. Sci.*, **62**, 1446–1462, doi:10.1175/JAS3412.1.

Rosenthal, S. L., 1965: Some preliminary theoretical considerations of tropospheric wave motions in equatorial latitudes. *Mon. Wea. Rev.*, **93**, 605–612, doi:10.1175/1520-0493(1965)093<0605:SPTCOT>2.3.CO;2.

Roundy, P. E., and W. M. Frank, 2004: A climatology of waves in the equatorial region. *J. Atmos. Sci.*, **61**, 2105–2132, doi:10.1175/1520-0469(2004)061<2105:ACOWIT>2.0.CO;2.

——, and M. A. Janiga, 2012: Analysis of vertically propagating convectively coupled equatorial waves using observations and a non-hydrostatic Boussinesq model on the equatorial beta-plane. *Quart. J. Roy. Meteor. Soc.*, **138**, 1004–1017, doi:10.1002/qj.983.

Schreck, C. J., J. Molinari, and A. Aiyyer, 2012: A global view of equatorial waves and tropical cyclogenesis. *Mon. Wea. Rev.*, **140**, 774–788, doi:10.1175/MWR-D-11-00110.1.

Sobel, A. H., and C. S. Bretherton, 1999: Development of synoptic-scale disturbances over the summertime tropical northwest Pacific. *J. Atmos. Sci.*, **56**, 3106–3127, doi:10.1175/1520-0469(1999)056<3106:DOSSDO>2.0.CO;2.

Straub, K. H., and G. N. Kiladis, 2003a: Extratropical forcing of convectively coupled Kelvin waves during austral winter. *J. Atmos. Sci.*, **60**, 526–543, doi:10.1175/1520-0469(2003)060<0526:EFOCCK>2.0.CO;2.

——, and ——, 2003b: Interactions between the boreal summer intraseasonal oscillation and higher-frequency tropical wave activity. *Mon. Wea. Rev.*, **131**, 945–960, doi:10.1175/1520-0493(2003)131<0945:IBTBSI>2.0.CO;2.

Takayabu, Y. N., 1994: Large-scale cloud disturbances associated with equatorial waves. Part I: Spectral features of the cloud disturbances. *J. Meteor. Soc. Japan*, **72**, 433–449.

——, and T. Nitta, 1993: 3-5 day-period disturbances coupled with convection over the tropical Pacific Ocean. *J. Meteor. Soc. Japan*, **71**, 221–246.

——, G. N. Kiladis, and V. Magaña, 2016: Michio Yanai and tropical waves. *Multiscale Convection-Coupled Systems in the Tropics: A Tribute to the Late Professor Yanai, Meteor. Monogr.*, No. 56, Amer. Meteor. Soc., doi:10.1175/AMSMONOGRAPHS-D-15-0019.1, in press.

Tindall, J. C., J. Thuburn, and E. J. Highwood, 2006a: Equatorial waves in the lower stratosphere. I: A novel detection method. *Quart. J. Roy. Meteor. Soc.*, **132**, 177–194, doi:10.1256/qj.04.152.

——, ——, and ——, 2006b: Equatorial waves in the lower stratosphere. II: Annual and interannual variability. *Quart. J. Roy. Meteor. Soc.*, **132**, 195–212, doi:10.1256/qj.04.153.

Tomas, R. A., and P. J. Webster, 1994: Horizontal and vertical structure of cross-equatorial wave propagation. *J. Atmos. Sci.*, **51**, 1417–1430, doi:10.1175/1520-0469(1994)051<1417:HAVSOC>2.0.CO;2.

Wallace, J. M., 1971: Spectral studies of tropospheric wave disturbances in the tropical western Pacific. *J. Appl. Meteor.*, **9**, 557–612.

——, and C. P. Chang, 1969: Spectrum analysis of large-scale wave disturbances in the tropical lower troposphere. *J. Atmos. Sci.*, **26**, 1010–1025, doi:10.1175/1520-0469(1969)026<1010:SAOLSW>2.0.CO;2.

——, and L. A. Chang, 1972: On the application of satellite data on cloud brightness to the study of tropical wave disturbances. *J. Atmos. Sci.*, **29**, 1400–1403, doi:10.1175/1520-0469(1972)029<1400:OTAOSD>2.0.CO;2.

Wang, B., and X. Xie, 1996: Low-frequency equatorial waves in vertically sheared zonal flow. Part I: Stable waves. *J. Atmos. Sci.*, **53**, 3424–3437, doi:10.1175/1520-0469(1996)053<0449:LFEWIV>2.0.CO;2.

Webster, P. J., and J. R. Holton, 1982: Cross-equatorial response to middle-latitude forcing in a zonally varying basic state. *J. Atmos. Sci.*, **39**, 722–733, doi:10.1175/1520-0469(1982)039<0722:CERTML>2.0.CO;2.

Wheeler, M., and G. Kiladis, 1999: Convectively coupled equatorial waves: Analysis of clouds in the wavenumber–frequency domain. *J. Atmos. Sci.*, **56**, 374–399, doi:10.1175/1520-0469(1999)056<0374:CCEWAO>2.0.CO;2.

——, G. N. Kiladis, and P. J. Webster, 2000: Large-scale dynamical fields associated with convectively coupled equatorial waves. *J. Atmos. Sci.*, **57**, 613–640, doi:10.1175/1520-0469(2000)057<0613:LSDFAW>2.0.CO;2.

——, and H. H. Hendon, 2004: An all-season real-time multivariate MJO index: Development of an index for monitoring and prediction. *Mon. Wea. Rev.*, **132**, 1917–1932, doi:10.1175/1520-0493(2004)132<1917:AARMMI>2.0.CO;2.

Yanai, M., 1963: Preliminary survey of large-scale disturbances over the tropical Pacific region. *Geofis. Int.*, **3**, 73–84.

——, and T. Maruyama, 1966: Stratospheric wave disturbances propagating over the equatorial Pacific. *J. Meteor. Soc. Japan*, **44**, 291–294.

——, and Y. Hayashi, 1969: Large-scale equatorial waves penetrating from the upper troposphere into the lower stratosphere. *J. Meteor. Soc. Japan*, **47**, 167–182.

——, and M. Murakami, 1970a: A further study of tropical wave disturbances by the use of spectrum analysis. *J. Meteor. Soc. Japan*, **48**, 185–197.

——, and ——, 1970b: Spectrum analysis of symmetric and antisymmetric equatorial waves. *J. Meteor. Soc. Japan*, **48**, 331–347.

——, and M.-M. Lu, 1983: Equatorially trapped waves at the 200 mb level and their association with meridional convergence of wave energy flux. *J. Atmos. Sci.*, **40**, 2785–2803, doi:10.1175/1520-0469(1983)040<2785:ETWATM>2.0.CO;2.

——, T. Maruyama, T. Nitta, and Y. Hayashi, 1968: Power spectra of large-scale disturbances over the tropical Pacific. *J. Meteor. Soc. Japan*, **46**, 291–294.

Yang, G.-Y., and B. Hoskins, 2013: ENSO impact on Kelvin waves and associated tropical convection. *J. Atmos. Sci.*, **70**, 3513–3532, doi:10.1175/JAS-D-13-081.1.

——, ——, and J. Slingo, 2003: Convectively coupled equatorial waves: A new methodology for identifying wave structures in observational data. *J. Atmos. Sci.*, **60**, 1637–1654, doi:10.1175/1520-0469(2003)060<1637:CCEWAN>2.0.CO;2.

——, ——, and ——, 2007a: Convectively coupled equatorial waves. Part I: Horizontal and vertical structures. *J. Atmos. Sci.*, **64**, 3406–3423, doi:10.1175/JAS4017.1.

——, ——, and ——, 2007b: Convectively coupled equatorial waves. Part III: Synthesis structures and their forcing and evolution. *J. Atmos. Sci.*, **64**, 3438–3451, doi:10.1175/JAS4019.1.

——, B. J. Hoskins, and J. M. Slingo, 2011: Equatorial waves in opposite QBO phases. *J. Atmos. Sci.*, **68**, 839–862, doi:10.1175/2010JAS3514.1.

——, B. Hoskins, and L. Gray, 2012: The influence of the QBO on the propagation of equatorial waves into the stratosphere. *J. Atmos. Sci.*, **69**, 2959–2982, doi:10.1175/JAS-D-11-0342.1.

Yasunaga, K., K. Yoneyama, Q. Moteki, M. Fujita, Y. N. Takayabu, J. Suzuki, T. Ushiyama, and B. Mapes, 2010: Characteristics of 3–4- and 6–8-day period disturbances observed over the tropical Indian Ocean. *Mon. Wea. Rev.*, **138**, 4158–4174, doi:10.1175/2010MWR3469.1.

Yokoyama, C., and Y. N. Takayabu, 2012: Relationships between rain characteristics and environment. Part II: Atmospheric disturbances associated with shallow convection over the eastern tropical Pacific. *Mon. Wea. Rev.*, **140**, 2841–2859, doi:10.1175/MWR-D-11-00251.1.

Zangvil, A., 1975: Temporal and spatial behavior of large-scale disturbances in tropical cloudiness deduced from satellite brightness data. *Mon. Wea. Rev.*, **103**, 904–920, doi:10.1175/1520-0493(1975)103<0904:TASBOL>2.0.CO;2.

——, and M. Yanai, 1980: Upper tropospheric waves in the tropics. Part I: Dynamical analysis in the wavenumber-frequency domain. *J. Atmos. Sci.*, **37**, 283–298, doi:10.1175/1520-0469(1980)037<0283:UTWITT>2.0.CO;2.

——, and ——, 1981: Upper tropospheric waves in the tropics. Part II: Association with clouds in the wavenumber-frequency domain. *J. Atmos. Sci.*, **38**, 939–953, doi:10.1175/1520-0469(1981)038<0939:UTWITT>2.0.CO;2.

Zhang, C., 1993: Laterally forced equatorial perturbations in a linear model. Part II: Mobile forcing. *J. Atmos. Sci.*, **50**, 807–821, doi:10.1175/1520-0469(1993)050<0807:LFEPIA>2.0.CO;2.

——, and P. J. Webster, 1992: Laterally forced equatorial perturbations in a linear model. Part I: Stationary transient forcing. *J. Atmos. Sci.*, **49**, 585–607, doi:10.1175/1520-0469(1992)049<0585:LFEPIA>2.0.CO;2.